Stress induces cytoprotective TDP-43 nuclear bodies through lncRNA *NEAT1*-promoted phase separation

Authors: Chen Wang[1,2,*], Yongjia Duan[1,2,*], Gang Duan[1,2,*], Zhiwei Ma[1,†], Kai Zhang[1,2], Xue Deng[1,2], Beituo Qian[1,2], Jinge Gu[1,2], Qiangqiang Wang[1], Shuang Zhang[1], Lin Guo[3], Cong Liu[1,2,§], and Yanshan Fang[1,2,6,§]

Affiliations:

[1]Interdisciplinary Research Center on Biology and Chemistry, Shanghai Institute of Organic Chemistry, Chinese Academy of Sciences, Shanghai 201210, China

[2]University of Chinese Academy of Sciences, Beijing, 100049, China,

[3]Department of Biochemistry and Molecular Biology, Thomas Jefferson University, Philadelphia, PA 19107, USA

*These authors contributed equally

[†]Current address: West China School of Basic Medical Sciences and Forensic Medicine, Sichuan University, Chengdu, 610041, China

[§]Correspondence to:

Cong Liu: liulab@sioc.ac.cn

Yanshan Fang: fangys@sioc.ac.cn

Tel: +86-21-6858.2510

Fax: +86-21-6858.2502

Short title (<50 characters): Phase-separated TDP-43 NBs mitigate stress

Keywords: TDP-43, nuclear body, RNP granule, phase separation, lncRNA *NEAT1*

Word count: *~6500 words (excluding the title page, abstract, references and figure legends)*

Graphic Abstract

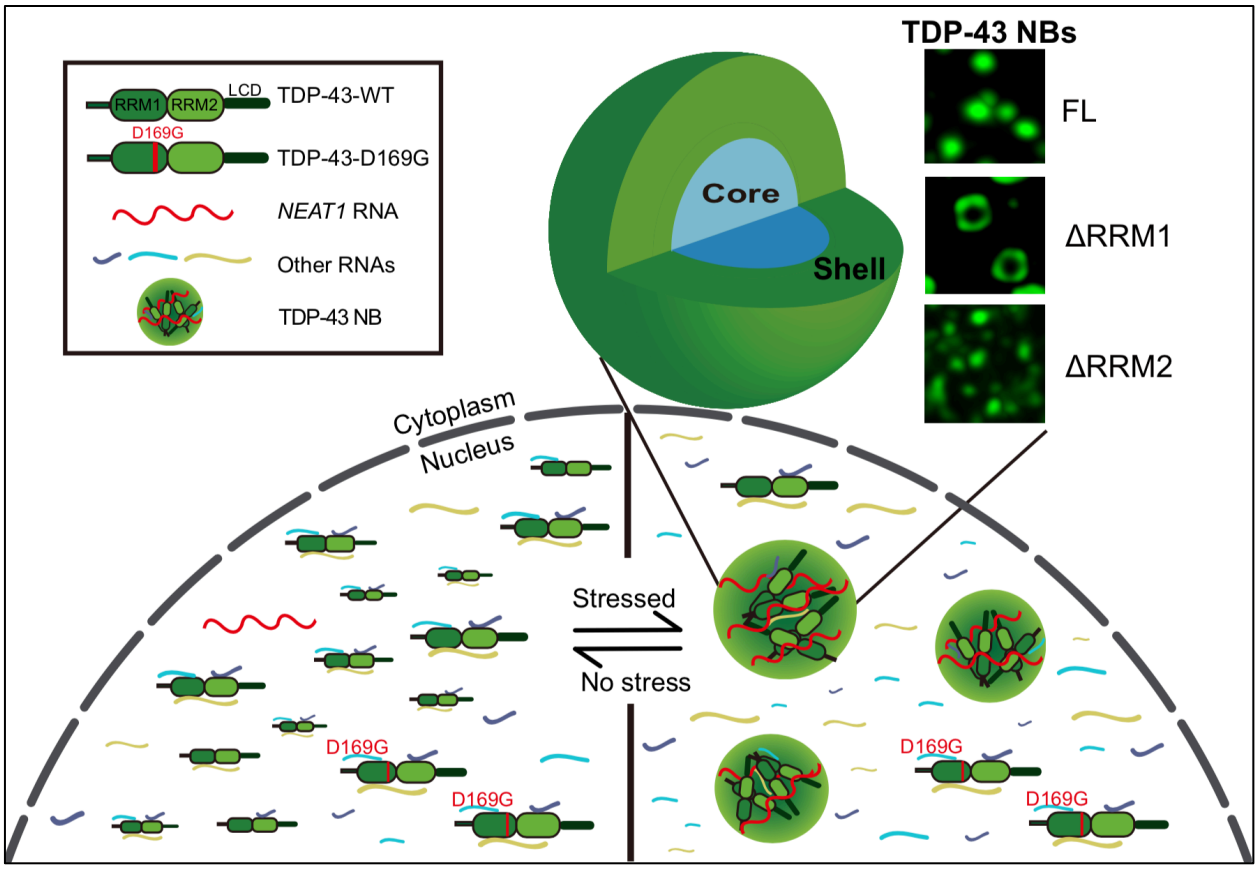

Highlights *(Up to four bullet points. The length of each highlight cannot exceed 85 characters, including spaces)*

- TDP-43 forms reversible, LD-like NBs alleviating cytotoxicity and neurodegeneration
- The two RRMs act antagonistically to maintain a core-shell architecture of TDP-43 NBs
- LncRNA *NEAT1* is upregulated in stressed neurons, which promotes TDP-43 LLPS
- ALS-causing mutation D169G abolishes *NEAT1*-induced TDP-43 LLPS and NBs

SUMMARY (< 150 words)

Despite the prominent role of TDP-43 in neurodegeneration, its physiological and pathological functions are not fully understood. Here, we report an unexpected function of TDP-43, which forms dynamic, reversible, droplet-like nuclear bodies (NBs) in response to stress, and the formation of NBs alleviates TDP-43-mediatd cytotoxicity and neurodegeneration in cell and *Drosophila* models of amyotrophic lateral sclerosis (ALS). Super-resolution microscopy reveals a "core-shell" architecture of TDP-43 NBs, which is maintained by the two RRMs antagonistically. Further, TDP-43 NBs are partially colocalized with nuclear paraspeckles and the paraspeckle scaffolding lncRNA *NEAT1* is dramatically upregulated in stressed neurons. Moreover, increase of *NEAT1* promotes TDP-43 liquid-liquid phase separation (LLPS) *in vitro*. Finally, we uncover that the ALS-associated mutation TDP-43^{D169G} impairs *NEAT1*-induced phase separation, causing a specific defect in the assembly of TDP-43 NBs but not stress granules. Together, our findings propose a stress-mitigating role and mechanism for TDP-43 NBs, whose dysfunction may contribute to ALS pathogenesis.

INTRODUCTION

Amyotrophic lateral sclerosis (ALS) is a progressive motor neuron disease characterized by the degeneration of motor neurons in the brain and spinal cord, which leads to fatal paralysis generally within 2–5 years after diagnosis (*1*,*2*). Missense mutations in the gene *TARDBP* encoding the trans-activation response element (TAR) DNA-binding protein 43 (TDP-43) predispose to familial ALS, and protein inclusions containing TDP-43 in the affected motor neurons are a pathological hallmark of ALS (*3*, *4*). TDP-43 is a nuclear protein but can shuttle between the nucleus and the cytoplasm. It has a nuclear localization signal (NLS), a nuclear export signal (NES), two canonical RNA recognition motifs (RRMs) that bind to nucleic acids, and a C-terminal low complexity domain (LCD) that mediates protein-protein interactions and is enriched of disease-associated mutations (*4*, *5*). TDP-43 is engaged in a variety of ribonucleoprotein (RNP) complexes and plays an important role in RNA processing and homeostasis (*6*-*10*). In addition, TDP-43 is known to participate in cytoplasmic stress granules (SGs), which may undergo aberrant phase transition and promote the formation of solid protein aggregates in diseased conditions (*11*-*14*).

Nuclear bodies (NBs) are dynamic, membraneless nuclear structures that concentrate specific nuclear proteins and RNAs and play an important role in maintaining nuclear homeostasis and RNA processing (*15*, *16*). Increasing evidence suggests the association of TDP-43 with a variety of NBs, such as paraspeckles (*17*-*19*), gemini of coiled bodies (GEMs) (*20*), nuclear stress bodies (*21*), interleukin-6 and -10 splicing activating compartment bodies (InSAC bodies) (*22*), and omega speckles (*23*). Notably, in the nucleus of spinal motor neurons of sporadic ALS patients, TDP-43 is found colocalized with paraspeckles and the occurrence of paraspeckles is specifically increased in the early phase of the disease (*18*). In addition, excessive formation of dysfunctional paraspeckles is also observed in the spinal neurons and glia of ALS-FUS patients (*24*). Although it is clear that TDP-43 is present in NBs that sometimes accompanies neurodegeneration, our understanding of the function of TDP-43 in NBs and the contribution of NBs to ALS pathogenesis is still rudimentary.

72 Recent studies indicate that liquid-liquid phase separation (LLPS) of RNA-binding protein
73 (RBPs) drives the assembly of liquid droplet (LD)-like, membraneless RNP granules in the
74 cytoplasm and nucleoplasm (*25-29*). Several ALS-related RBPs including TDP-43, FUS, hnRNP
75 A1, hnRNP A2 and TIA1 are shown to phase separate *in vitro* (*14*, *30-35*). The intrinsically
76 disordered LCD domains of the RBPs are thought to mediate the LLPS (*28*, *31*, *36-38*) and
77 posttranslational protein modifications play an important role in determining the biophysical and
78 biological properties of the phase behavior of the RBPs (*34*, *39-46*). In addition to the LCD,
79 recent studies reveal that RNA is of vital importance in regulating the LLPS (*47*, *48*), which can
80 either suppress or promote phase separation depending on the contents and concentrations of
81 the RNAs (*25*, *49-51*).

82 In this study, we find that various cellular stresses induce TDP-43 to form distinct, highly
83 dynamic and reversible NBs, which not only attenuate the cytotoxicity of TDP-43 in mammalian
84 cells but also ameliorate neurodegeneration and behavioral deficits in a *Drosophila* model of ALS.
85 Further investigation with super-resolution microscopy reveals the unexpected opposing
86 functions of the two RRMs in maintaining the core-shell architecture of TDP-43 NBs.
87 Furthermore, we demonstrate a crucial role of the paraspeckle scaffolding RNA nuclear-enriched
88 abundant transcript 1 (*NEAT1*) in promoting TDP-43 LLPS *in vitro*, which is compromised by the
89 ALS-causing mutation D169G, leading to a defect in forming TDP-43 NBs. Together, our findings
90 demonstrate how stress induces the assembly of TDP-43 NBs in the generally “suppressive”
91 nucleoplasm environment and suggest the involvement of dysfunctional TDP-43 NBs in ALS
92 pathogenesis.

93 **RESULTS**

94 **Arsenic stress induces dynamic and reversible TDP-43 NBs**

95 TDP-43 protein is predominantly localized to the nucleus but can shuttle between the nucleus
96 and the cytoplasm. In response to cellular stress, TDP-43 is recruited to cytoplasmic SGs (*11*).
97 Interestingly, in an earlier related work of our group (*46*), we noticed that although arsenite, a
98 commonly used experimental reagent to raise cellular stress (*52*), induced TDP-43^{+} cytoplasmic
99 SGs, the majority of TDP-43 signal remained in the nucleus. Furthermore, in a great portion of
100 the cells, the nuclear TDP-43 lost the normal diffused pattern and instead exhibited a distinct
101 granular appearance (Movie S1 and Fig. 1, A and B).

102 A membraneless nuclear structure fulfills the requirements of NBs if it is: (1) microscopically
103 visible, (2) enriched with specific nuclear factors, and (3) continuously exchanging the contents
104 with the surrounding nucleoplasm (*15*). Indeed, arsenite-induced TDP-43 nuclear granules were
105 microscopically visible (Fig. 1). Further examination by immunocytochemistry indicated that
106 these arsenite-induced nuclear granules were colocalized or partially colocalized with several
107 known types of NBs, especially paraspeckles marked by splicing factor proline-glutamine rich
108 (SFPQ) (Fig. S1). These results suggest that cellular stress may be involved in the translocation
109 of TDP-43 into NBs such as paraspeckles, similar to that found in the spinal motor neurons of
110 ALS patients (*18*).

111 To examine if stress-induced TDP-43 nuclear granules were liquid-like and could exchange
112 with surrounding nucleoplasm, we performed the fluorescence recovery after photobleaching
113 (FRAP) analysis in *live* cells using a green fluorescent protein (GFP)-tagged TDP-43
114 (GFP-TDP-43). To induce TDP-43 nuclear granules, cells were pre-treated with arsenite (250 μM)
115 for 30 minutes before photobleaching. The fluorescence of GFP-TDP-43 nuclear granules was
116 rapidly recovered after photobleaching, reaching ~50% of the pre-bleaching intensity in ~65
117 seconds (Movie S2 and Fig. 1, C and D). Thus, these data indicate that stress-induced TDP-43
118 nuclear granules are liquid-like and highly dynamic. Together, they fulfilled all the above three
119 requirements and are thereafter called TDP-43 NBs in this study.

120 Next, we determined whether stress-induced TDP-43 NBs were reversible using arsenite
121 washout assay. After arsenite removal, the stress-induced TDP-43 NBs gradually disappeared
122 and eventually recovered to nearly diffused pattern like that before the arsenite treatment (Fig.
123 1E). Our quantitative analyses indicated that both the percentages of cells with TDP-43 NBs and
124 the number of TDP-43 NBs per cell decreased in a time-dependent manner after arsenite
125 washout (Fig. 1, F to H). Of note, there were considerably more cells with TDP-43 NBs than
126 TDP-43-associated (TDP-43$^+$) SGs (Fig. 1B) and overwhelmingly more TDP-43 NBs than
127 TDP-43$^+$ SGs per cell before the washout started (Fig. 1E, 0 min). Hence, although the
128 percentages of cells with visible TDP-43 NBs were not markedly reduced when TDP-43$^+$ SGs
129 became largely undetectable at 30 min after arsenite removal (Fig. 1, F and G), the average
130 number of TDP-43 NBs per cell did significantly decrease (Fig. 1H). Together, our data indicate
131 that arsenic stress-induced TDP-43 NBs are reversible as that of SGs upon the relief of stress.
132

133 **Formation of TDP-43 NBs as a general cellular stress mechanism**

134 Next, we examined if endogenous TDP-43 could also form NBs upon arsenic stress. We found
135 that in most cells, endogenous TDP-43 was present as evenly distributed while some cells
136 showed spontaneous small granules (Fig. S2A). The arsenite treatment led to the formation of
137 larger and more NBs in a significantly increased number of cells (Fig. S2, A and B). In addition,
138 we observed stress-induced TDP-43 NBs also in *in vitro* cultured mouse primary neurons (Fig.
139 S2, C and D). Thus, the formation of TDP-43 NBs is not an artificial effect due to TDP-43
140 overexpression or the use of non-neuronal cell lines. Moreover, it was previously reported that
141 heat shock-induced reversible nuclear TDP-43 “aggregations” were colocalized with the marker
142 of nuclear stress bodies (*21*). These observations raised the possibility that the formation of
143 TDP-43 NBs might be a general stress response mechanism in the nucleus. Indeed, we found
144 that disturbance of the nuclear homeostasis by inhibiting nuclear export with leptomycin B (LMB)
145 also effectively induced endogenous TDP-43 to form NBs (Fig. 2, A and B).

146 To further determine whether blocking nuclear export of TDP-43 itself was sufficient to
147 induce the formation of TDP-43 NBs, we generated mutations in the NLS and the NES of
148 TDP-43, respectively (NLS^{mut} and NES^{mut}; Fig. 2C). Under normal conditions, wild-type (WT)
149 TDP-43 was mostly present in diffused pattern in the nucleus with rare occurrence of
150 spontaneous TDP-43 NBs (Fig. 2, D to F). As expected, the NLS^{mut} TDP-43 was predominantly
151 cytoplasmic and thus the chance of TDP-43 NBs with the NLS^{mut} was even lower than that of the
152 WT (Fig. 2, D to F). In contrast, the NES^{mut} was exclusively nuclear and formed TDP-43 NBs
153 even in the absence of arsenite, heat shock or LMB treatment (Fig. 2, D to F). Furthermore, the
154 solubility of TDP-43-NES^{mut} protein was significantly reduced, as more than half of the protein
155 was insoluble in radioimmunoprecipitation assay buffer (RIPA) (Fig. 2, G and H).

156 The marked reduction in the solubility of the NES^{mu} protein raised the question whether the
157 TDP-43-NES^{mut} NBs were still in a dynamic, liquid-like state or became solid "aggregates". To
158 address this question, we examined the stability of WT and mutant TDP-43 proteins by treating
159 cells with protein synthesis inhibitor cycloheximide (CHX) (*53*). We found that the RIPA-soluble
160 TDP-43 protein was rather stable, as none of the WT, NLS^{mut} or NES^{mut} TDP-43 in the soluble
161 fractions showed significant turnover in 24 h after CHX treatment (Fig. S3, A to D). In contrast,
162 the RIPA-insoluble fraction of TDP-43-NES^{mut} decreased rapidly upon CHX inhibition and
163 became almost undetectable within 24 h (Fig. S3, A to D). Meanwhile, we found that the
164 treatment with CHX led to rapid disassembly of TDP-43-NES^{mut} NBs and reduction in the number
165 of TDP-43-NES^{mut} NBs per cell (Fig. S3, E and F). These results suggest that the RIPA-insoluble
166 TDP-43-NES^{mut} NBs are in a reversible, liquid-like state rather than solid "aggregates". A similar
167 observation of misfolded proteins entering the liquid-like, granular nucleolus under stress was
168 recently reported, which may function as a phase-separated protein quality control compartment
169 (*54*).

170 Next, we further examined how disturbance of the cellular proteostasis by blocking protein
171 turnover impacted on this process. We inhibited proteasome-mediated protein degradation by
172 MG132, which led to a significant increase in the RIPA-insoluble fraction of the NES^{mut} as well as

173 that of the WT TDP-43 protein (Fig. S4, A to D). In contrast, blocking autophagic flux by
174 chloroquine (CQ) did not significantly affect the levels of insoluble TDP-43 (Fig. S4, E to H). Thus,
175 the turnover of TDP-43 NBs did not rely on the autophagy-lysosomal pathway, which was more
176 commonly used to clear misfolded protein aggregates (*55*, *56*). Together, our data indicate that
177 TDP-43 NBs are dynamic, reversible and sensitive to the environment of surrounding
178 nucleoplasm, which may act as a general cellular mechanism to various stresses.
179

180 **Formation of TDP-43 NBs alleviates the cytotoxicity**

181 We were keen to understand the functional significance of forming TDP-43 NBs. Was it a
182 "protective" mechanism for cells, like that of SGs? Indeed, we found that overexpression (OE) of
183 WT or NLS^{mut} TDP-43 but not the NB-forming NES^{mut} in human 293T cells led to decreased cell
184 viability (Fig. 3A). To further confirm that the formation of TDP-43 NBs was required for the
185 cytotoxicity-antagonizing effect rather than simply restricting TDP-43 in the nucleus, we sought
186 for alternative approaches to promote or suppress TDP-43 NBs without disrupting its
187 nucleocytoplasmic transport. It was previously shown that an acetylation-mimic K145/192Q
188 mutation of TDP-43 impaired the RNA-binding and promoted the formation of TDP-43 protein
189 inclusions in both the nucleus and the cytoplasm, whereas the acetylation-deficient K145/192R
190 mutation suppressed that (*40*). Hence, we generated the K145/192Q mutation in WT TDP-43
191 (Fig. 3B) and the K145/192R mutation in TDP-43-NES^{mut} (Fig. 3C).

192 Indeed, the K145/192Q mutation led to the formation of TDP-43 NBs without affecting the
193 nucleocytoplasmic distribution of TDP-43 and that was in the absence of LMB or arsenite
194 treatment (Fig. 3, D, D', F, and H). And importantly, the NB-promoting K145/192Q mutation
195 alleviated the cytotoxicity of WT TDP-43 (Fig. 3J), similar to the effect of the NES^{mut} (Fig. 3A). On
196 the other hand, abolishing NB formation of the NES^{mut} by the K145/192R mutation (Fig. 3, E, E',
197 G, and I) made the originally non-toxic TDP-43-NES^{mut} to exhibit marked cytotoxicity (Fig. 3K),
198 like that of the WT TDP-43 (Fig. 3A). These data demonstrate that the formation of TDP-43 NBs

199 reduces the cytotoxicity and increases the cell viability, therefore potentially acting as a
200 "protective" mechanism to help cells survive stressed or diseased conditions.
201

202 **TDP-43-NES^{mut} forms neuronal NBs *in vivo* and mitigates neurodegeneration in a**
203 ***Drosophila* model of ALS**

204 To validate our findings in an *in vivo* model, we utilized the binary GAL4-UAS system (*57*) to
205 generate transgenic flies in order to express WT, NLS^{mut} or NES^{mut} human TDP-43 (hTDP-43) in
206 a tissue-specific manner. The transgenes of WT and mutant UAS-*hTDP-43* were inserted in the
207 same locus of the fly genome by ΦC31 integrase-mediated, site-specific integration (*58-60*). This
208 approach avoided the location effect on transgene expression across different fly lines and
209 allowed direct comparison between the WT and mutant TDP-43 flies. Immunohistochemistry
210 analysis of the whole mount fly brains confirmed the predominant nuclear localization of the WT
211 and NES^{mut} hTDP-43 in the fly neurons (*elav*-Gal4), whereas the NLS^{mut} was largely cytoplasmic
212 (Fig. 4A). Consistent with the data in 293T cells (Fig. 2, D to F), the NES^{mut} hTDP-43 formed
213 striking NBs in the nucleus of fly neurons (Fig. 4, A and B). Furthermore, the solubility of the
214 hTDP-43-NES^{mut} protein extracted from the fly brains was significantly decreased (Fig. 4, C and
215 D), which was also consistent with the results in the mammalian cells (Fig. 2, G and H).

216 We then examined the consequence of expressing WT, NLS^{mut} or NES^{mut} hTDP-43 in the fly
217 eye (GMR-Gal4). WT and NLS^{mut} hTDP-43 flies showed slight eye degeneration at Day 5, as
218 evidenced by the rough surface of the compound eyes and loss of pigment cells. At the same
219 time point, however, the eyes of the NES^{mut} flies were largely unaffected and the degeneration
220 score was much lower (0.4 ± 0.34) than that of WT hTDP-43 flies (1.5 ± 0.41, $P < 0.001$) (Fig. 4E).
221 By Day 25, the eyes of WT and NLS^{mut} hTDP-43 flies further degenerated as a lot more pigment
222 cells were lost and some eyes showed swelling especially in the NLS^{mut} hTDP-43 flies.
223 Compared to WT hTDP-43 flies (2.5 ± 0.13), the eye degeneration of the NLS^{mut} flies was
224 significantly worse (3.8 ± 0.17, $P < 0.001$), whereas that of the NES^{mut} flies was substantially
225 milder (0.8 ± 0.14, $P < 0.001$) (Fig. 4E). Similar conclusions were obtained from the climbing

226 assay, which also showed a striking difference in the severity of neurotoxicity among WT, NLS^{mut}
227 and NES^{mut} hTDP-43 flies. Expression of WT hTDP-43 in the fly motor neurons (D42-Gal4)
228 caused an age-dependent decline of the climbing capability, which deteriorated much faster in
229 the NLS^{mut} flies (Fig. 4F). The behavioral phenotype of NES^{mut} flies was the mildest, whose
230 climbing capability was not statistically different from that of the control flies (UAS-*Luciferase*) at
231 all time points examined (Fig. 4F). Together, these data indicate that the formation of TDP-43
232 NBs by the NES^{mut} alleviates the TDP-43-mediated neurodegeneration in an *in vivo Drosophila*
233 model of ALS.
234

235 **The role of the major functional domains of TDP-43 in the assembly of NBs**

236 To understand how TDP-43 NBs were assembled, we generated truncated TDP-43 proteins,
237 namely ΔLCD, ΔRRM1 and ΔRRM2, to determine how each major domain of TDP-43 is involved
238 in regulating this process (Fig. S5A). It was previously shown that the intrinsically disordered
239 LCD domain mediated protein-protein interaction and was critical for the formation of cytoplasmic
240 SGs and protein aggregations (*31*, *61*). We found that both the WT and ΔLCD TDP-43 were
241 mostly soluble (Fig. S5, B and C), however, the ΔLCD was unable to form NBs in response to
242 LMB (Fig. S5, F to G'), indicating that the formation of TDP-43 NBs in cells requires the LCD
243 domain.

244 Next, we examined the impact of deleting RRM1 or RRM2 on the assembly of TDP-43 NBs.
245 The ΔRRM1 TDP-43 was largely soluble (Fig. S5D), while the ΔRRM2 showed a greatly
246 increased insolubility (Fig. S5E). Interestingly, the ΔRRM1 TDP-43 formed large, ring-like
247 structures in the nucleus even in the absence of LMB treatment (Fig. S5H). And, treatment with
248 LMB did not promote further formation of the ring-like structures or trigger the formation of
249 WT-like TDP-43 NBs (Fig. S5H'). ΔRRM2 TDP-43 looked similar to WT in cells without stress
250 (Fig. S5I), whereas treating with LMB gave rise to a grainy appearance (Fig. S5I').
251

252 **Super-resolution microscopy reveals a "core-shell" architecture of TDP-43 NBs**
253 **maintained by the opposing functions of the two RRMs**

254 To further characterize the nuclear structures formed by WT, ΔRRM1 and ΔRRM2 TDP-43, we
255 utilized the Leica LIGHTNING SP8 confocal microscope to capture multicolor images in
256 super-resolution down to 120 nm. Interestingly, we found that WT TDP-43 formed solid, mid-size
257 NBs; ΔRRM1 was much larger, ring-shaped; and ΔRRM2 displayed a mesh-like structure with
258 many smaller NBs (Fig. 5, A and B). Three-dimensional (3D) rendering revealed that WT TDP-43
259 NBs were not perfect "spheres" as ones might infer from the 2D images; rather, they were in oval
260 or cylinder shapes in the cell. Unlike WT TDP-43, ΔRRM1 was mostly large, hollow "pillars";
261 whereas ΔRRM2 NBs looked similar to those of WT in 3D rendering. Further quantification
262 confirmed that the average diameter of ΔRRM1 "rings" was drastically larger whereas that of
263 ΔRRM2 NBs was noticeably smaller than that of WT TDP-43 (Fig. 5C).

264 Given the distinct morphology of the nuclear structures formed by ΔRRM1 and ΔRRM2
265 TDP-43, it was tempting to propose a "core-shell" architecture of TDP-43 NBs and the two RRMs
266 might function antagonistically to maintain such a structure – the RRM1 pushed TDP-43 toward
267 the core of NBs whereas the RRM2 pulled TDP-43 toward the shell (Fig. 5D). If this hypothesis
268 were correct, ΔRRM1 TDP-43 that lacked the "centripetal force" of the RRM1 would be mainly
269 distributed to the shell of NBs, while ΔRRM2 TDP-43 that lacked the "centrifugal force" would be
270 mainly located in the core. To test this hypothesis, we co-expressed HA-Tagged WT TDP-43
271 with Myc-tagged WT, ΔRRM1 or ΔRRM2 TDP-43 and induced NB formation in 293T cells by
272 LMB (Fig. 5, E to H). Indeed, ΔRRM1 formed a ring-like shell wrapping the co-expressed WT
273 TDP-43 NBs (Fig. 5, F and J) and the diameter of the NBs was dramatically larger (Fig. 5N). The
274 increased diameter was not simply due to overexpression of two folds of TDP-43 protein, as
275 co-expression of WT TDP-43-HA and WT myc-TDP-43 did not show such effect (Fig. 5, E, I, and
276 M). Consistent with our hypothesis, we found that ΔRRM2 co-expressed with the WT TDP-43
277 was mainly located in the core of NBs (Fig. 5, G and K) and the diameter was significantly
278 smaller (Fig. 5O). The core-shell architecture could also be clearly seen when ΔRRM1 and

279 ΔRRM2 TDP-43 were co-expressed (Fig. 5, H, L, and P). Therefore, the data suggest that RRM1
280 and RRM2 play different or even opposing functions in the assembly of TDP-43 NBs, possibly by
281 interacting with different RNAs and other RNA-binding NB proteins via the different RRMs.
282

283 **RNA suppresses TDP-43 *in vitro* de-mixing via the RRMs**

284 Recent studies indicate that the de-mixing process by LLPS condenses RBPs into LD-like
285 compartments, allowing for the formation of intracellular membraneless RNP granules (*25-29*).
286 Several ALS-related RBPs including TDP-43, FUS, hnRNP A1, hnRNP A2 and TIA1 have been
287 shown to phase separate *in vitro* (*14*, *30-35*). The dynamic, reversible and membraneless
288 characteristics of TDP-43 NBs suggested that LLPS might be involved in the formation of
289 TDP-43 NBs. Indeed, we found that purified full-length (FL) TDP-43 underwent LLPS and formed
290 LDs *in vitro* in a dose-dependent manner (Fig. S6, A to C). Similar to the observation in cells (Fig.
291 S5, G and G'), the C-terminal LCD truncation (TDP-43$^{1-274}$) showed greatly reduced LLPS
292 capability (Fig. S6D), suggesting a major role of the LCD in mediating TDP-43 de-mixing *in vitro*
293 and *in vivo*. Nevertheless, the formation of TDP-43$^{1-274}$ LDs was evident at a higher protein
294 concentration (50 μM) (Fig. S6D), confirming the previous observation that the N-terminal
295 domains of TDP-43 could drive LLPS *in vivo* (*32*).

296 To gain insights into the mechanism involved in the regulation of TDP-43 NBs, we
297 determined how RNA impacts on the LLPS of TDP-43 by adding total RNAs extracted from HeLa
298 cells into the *in vitro* de-mixing system (Fig. S6, E and F). The addition of total RNAs markedly
299 reduced the LLPS of FL TDP-43 at a concentration of 500 ng/μl (Fig. S6E), whereas a much
300 lower concentration of total RNAs (100 ng/μl) was sufficient to suppress the LLPS of TDP-43$^{1-274}$
301 (Fig. S6F). These results confirm the predominant LLPS-promoting role of the C-terminal LCD
302 and suggest an LLPS-suppressing function for the N-terminal RNA-binding regions. We then
303 moved on to test how the two RRMs were involved in the RNA suppression of TDP-43 LLPS.
304 Since the LLPS-promoting effect of the LCD in TDP-43 was overwhelming and made the function
305 of the RRMs in RNA suppression difficult to assess in the *in vitro* de-mixing assay (Fig. S6, E and

306 F), we instead generated and tested ΔRRM1 and ΔRRM2 TDP-43$^{1-274}$ proteins (Fig. 6A and Fig.
307 S6G). We confirmed that the RNA-binding affinity of ΔRRM1 and ΔRRM2 TDP-43$^{1-274}$ was
308 significantly reduced (Fig. S6, H and I). WT as well as ΔRRM1 and ΔRRM2 TDP-43$^{1-274}$ formed
309 LDs by LLPS *in vitro* in a dose-dependent manner, though the de-mixing of ΔRRM1 TDP-43$^{1-274}$
310 appeared less robust than that of WT or ΔRRM2 (Fig. S6, J to L).

311 To better compare the difference in RNA suppression, we lowered the NaCl concentration
312 and increased the crowding agent PEG, which allowed WT TDP-43$^{1-274}$ to form larger LDs (Fig.
313 6B). We found that total RNAs at a concentration of 100 ng/μl markedly reduced the size and
314 number of LDs of WT TDP-43$^{1-274}$. ΔRRM1 TDP-43$^{1-274}$ did not form large LDs as WT at the
315 concentration of 50 μM and we initially thought its LLPS would be more easily suppressed by
316 total RNAs. To our surprise, a much higher concentration (500 ng/μl) of total RNAs was required
317 to see effective suppression (Fig. 6C), suggesting that deletion of the RRM1 greatly reduced the
318 ability of total RNAs to suppress the formation of TDP-43 droplets, which was consistent with the
319 finding that ΔRRM1 TDP-43 spontaneously phase separated into ring-like nuclear structures in
320 cells even in the absence of cellular stress (Fig. S5H). We also tested ΔRRM1 TDP-43$^{1-274}$ at 100
321 μM to allow large ΔRRM1 LDs to form and the result confirmed that the suppression of TDP-43
322 LLPS by total RNAs was dramatically reduced with ΔRRM1, requiring total RNAs of about 250
323 ng/μl (Fig. 6C'). The suppression of the LLPS of ΔRRM2 TDP-43$^{1-274}$ by total RNAs (100~250
324 ng/μl) was slightly reduced compared to that of WT (Fig. 6, B and D), but to a less extent than
325 that of ΔRRM1 (Fig. 6, C and C'). It was worth noting that ΔRRM1 TDP-43$^{1-274}$ showed both
326 decreased LLPS capacity and reduced sensitivity to RNA suppression, indicating that a RBP
327 with a lower tendency to phase separate on its own does not necessarily makes its LLPS more
328 sensitive to RNA suppression. Nevertheless, these data indicate that both RRMs are involved in
329 RNA suppression of TDP-43 LLPS.

330

331 **Upregulation of *NEAT1* RNA promotes TDP-43 LLPS**

332 Recent works have revealed both positive and negative regulation of LLPS of prion-like

333 RBPs by RNA (*62*). For example, tRNA was shown to reduce the LLPS of FUS *in vitro* (*50*).
334 Similarly, tRNA also potently suppressed the *in vitro* LLPS of TDP-43 (Fig. 6E). We further
335 examined the function of the two RRMs in mediating tRNA suppression. We found that ΔRRM1
336 TDP-43^{1-274} showed similar sensitivity to tRNA suppression, as 1.25 μg/μl of tRNA was sufficient
337 to suppress the LLPS of both WT and ΔRRM1 TDP-43^{1-274} (Fig. 6, E and F). At this condition,
338 however, ΔRRM2 LDs could still be observed and the effective suppression required a higher
339 concentration of tRNA (2.5 μg/μl). It should be pointed out that, unlike the response to total RNAs,
340 ΔRRM1 TDP-43^{1-274} did not exhibit a greatly decreased sensitivity to tRNA suppression, despite
341 that again only small ΔRRM1 LDs were present at the beginning of the suppression test. Thus,
342 the lack of a strong suppression of ΔRRM1 LLPS by total RNAs (Fig. 6C) was not simply
343 because suppression of small LDs was difficult to detect.

344 Since stress-induced TDP-43 NBs were co-localized with paraspeckles (Fig. S1, A and B)
345 and TDP-43 bound directly to the paraspeckle scaffolding RNA *NEAT1* (*18*, *63*), we next
346 examined whether *NEAT1* RNA impacted on the phase behavior of TDP-43. Interestingly, we
347 found that *NEAT1* promoted the LLPS of TDP-43 in a dose-dependent manner (Fig. 6H), and
348 this regulation by *NEAT1* required both the RRM1 and RRM2 of TDP-43 (Fig. 6, I and J).
349 Furthermore, we showed that increasing concentrations of *NEAT1* antagonized the suppressing
350 effect of tRNA, inducing the formation of TDP-43 droplets *in vitro* (Fig. 6K). In this suppressive
351 environment, the *NEAT1*-mediated induction of the LLPS of ΔRRM1 TDP-43^{1-274} was markedly
352 reduced (Fig. 6L), which was consistent with the observations that ΔRRM1 TDP-43 remained
353 soluble and LMB did not promote the formation of NBs or increase the number of the ring-like
354 nuclear structures in cells (Fig. S5, D, H and H'). Under the same condition, *NEAT1* RNA more
355 readily induced the *in vitro* de-mixing of ΔRRM2 TDP-43^{1-274} (Fig. 6M), likely because tRNA
356 suppression of ΔRRM2 was less effective (Fig. 6G). The overall increased tendency to form LDs
357 and to remain phase separated might underlie the formation of more condensed, insoluble
358 TDP-43 NBs by ΔRRM2 (Fig. S5, E, I and I').

359 Given that *NEAT1* RNA could act as scaffolds to promote the nucleation of paraspeckles (*50*,
360 *64-67*) and that stress-induced TDP-43 NBs were partially co-localized with paraspeckles (Fig.
361 S1, A and B), our data strongly suggest that *NEAT1* plays an important role in triggering the
362 formation of stress-induced TDP-43 NBs in cells. Supporting this hypothesis, we found that the
363 levels of both the total *NEAT1* RNA and the long non-coding RNA (lncRNA) isoform *NEAT1_2*
364 were dramatically increased in mouse primary neurons treated with arsenite (Fig. 6N) or LMB
365 (Fig. 6O), consistent with the observation earlier in this study that TDP-43 formed NBs in
366 stressed neurons (Fig. S2, C and D). Together, we propose that cellular stress increases NEAT1
367 RNA levels, which antagonize the suppressive environment of the nucleoplasm by providing
368 nucleation scaffolds that condensate TDP-43 and other NB components, triggering the formation
369 of TDP-43 NBs in stressed cells.
370

371 **ALS-associated D169G mutation of TDP-43 shows a specific defect in NB formation**

372 This study was launched by the discovery that TDP-43 formed cytotoxicity-antagonizing NBs in
373 mammalian cells and the formation of NBs alleviated TDP-43-mediated neurodegeneration in
374 flies. To further investigate the relevance of TDP-43 NBs in the pathogenesis of human diseases,
375 we examined several known ALS-causing TDP-43 mutants. Interestingly, we found that the
376 mutation of D169G (640A>T) (*4*; and Fig. 7A) dramatically reduced the capability of TDP-43 to
377 form NBs in response to stress induced by arsenite (Fig. 7, B to D) or LMB (Fig. S7, A to C). In
378 contrast, the nucleocytoplasmic transport and recruitment of D169G TDP-43-D169G to SGs was
379 unaffected (Fig. 7, B and E), which was consistent with the previous assessments of D169G in
380 SG formation (*68*, *69*). The D169G mutation is in the RRM1, which is thought to cause a local
381 conformational change that increases the thermal stability of the RRM1 (*70*, *71*). It is worth
382 noting that most known disease-associated mutations such as M337V are enriched in the LCD
383 region of TDP-43 (Fig. S7, D and E), which are thought to promote aberrant phase transition of
384 SGs to irreversible protein aggregates in disease (*11*). Unlike D169G, we did not observe a
385 significant effect of M337V mutation on the assembly of TDP-43 NBs (Fig. S7, F and G). Thus,

386 TDP-43^{D169G} has a specific defect in the formation of stress-induced NBs. In addition, these
387 findings indicate that although TDP-43 NBs and SGs are both phase-separated RNP granules,
388 the exact mechanisms regulating their assembly are different.

389 Next, we examined if the phase separation behavior of TDP-43-D169G was altered, which
390 might contribute to the defect in TDP-43 NB formation. We found that purified D169G TDP-43$^{1-274}$
391 protein formed LDs in a dose-dependent manner just like that of WT in the *in vitro* LLPS assay
392 (Fig. 7, F, G and H), suggesting that the ability of D169G to phase separate was not dramatically
393 changed. Further, the suppression of TDP-43 LLPS by total RNAs showed no difference in
394 D169G compared to that of WT TDP-43$^{1-274}$ (Fig. 7, I and J), suggesting the normal regulation of
395 TDP-43 RNP granules by total RNAs remained intact in D169G. This was consistent with the
396 result that D169G did not affect SG assembly or TDP-43 translocation to SGs (Fig. 7B and 7E).
397 In striking contrast, the induction of TDP-43 LLPS by *NEAT1* RNA was drastically reduced in
398 D169G (Fig. 7, K and L). Thus, these data not only well cohered with the observation that
399 TDP-43-D169G was defective in NB formation but also further confirmed the crucial role of
400 *NEAT1* in triggering the assembly of TDP-43 NBs. Together with the cytotoxicity-antagonizing
401 function of TDP-43 NBs (Fig. 3 and Fig. 4), the findings of D169G (Fig. 7) suggest that a
402 compromise of stress-induced TDP-43 NBs may be involved in ALS pathogenesis.

403 **DISCUSSION**

404 This study was initiated by the finding that TDP-43 formed distinct nuclear granules in stressed
405 cells. We then characterized these subnuclear structures and demonstrated that they meet the
406 three criteria of NBs (*15*) – (1) microscopically distinctive; (2) enriched of TDP-43 and partially
407 colocalized with paraspeckles; and (3) liquid or hydrogel-like, highly dynamic and sensitive to the
408 surrounding nucleoplasm. Further, we show that various cellular stresses such as arsenic stress,
409 nuclear export blockage and proteasomal inhibition induce the formation of TDP-43 NBs. And
410 TDP-43 NBs are detected in human cells, mouse primary neurons, and fly brains *in vivo*. Thus,
411 the assembly of TDP-43 NBs may be a general stress response that occurs in multiple cell types
412 and different organisms.
413

414 **The cytotoxicity-antagonizing effect of TDP-43 NBs**

415 Although TDP-43 insoluble aggregates are found in the nucleus and cytoplasm of affected
416 neurons in ALS and FTD patients, reducing TDP-43 aggregates did not reduce or prevent cell
417 death (*72*), suggesting that TDP-43 aggregation is associated with rather than a primary cause of
418 neurodegeneration. Interestingly, we find in this study that NB-forming TDP-43 such as the
419 NES^{mut} and the K145/192Q mutation are much less cytotoxic than diffused WT TDP-43. More
420 importantly, abolishing the capability of TDP-43-NES^{mut} to form NBs makes the originally
421 non-toxic NES^{mut} exhibit cytotoxicity. Furthermore, transgenic flies expressing TDP-43-NES^{mut}
422 form remarkable NBs in the fly neurons and the neurodegeneration is considerably less severe
423 than that of the TDP-43-WT flies. In line of the cytoprotective role, TDP-43^{+} paraspeckles are
424 observed in the spinal motor neurons of ALS patients especially in the early phases of the
425 disease (*18*), suggesting that TDP-43 NBs may be called up and engaged in the first line of
426 defense against cellular stress and disease conditions.

427 Paraspeckles are a class of subnuclear RNP granules formed by the scaffolding lncRNA
428 *NEAT1* associated with SFPQ and other paraspeckle proteins (*64*, *66*, *73-75*), which are
429 engaged in regulating different cellular functions through nuclear retention of specific mRNAs

430 and proteins (*76-78*). SGs sequester mRNAs and temporarily arrest protein synthesis to help
431 cells survive stress (*79*). Given that TDP-43 is presented in both paraspeckles and SGs and
432 plays an important role in regulating gene expression and RNA metabolism (*63*, *80-82*), it is
433 reasonable to speculate that a similar underpinning mechanism may contribute to the
434 cytoprotective function of TDP-43 NBs. For example, assembly of TDP-43 NBs may stall DNA
435 transcription and/or arrest RNA processing; when stress is relieved, TDP-43 NBs disassemble
436 and release the RNAs and nuclear proteins required for normal cell functions. In addition, since
437 intranuclear inclusions of TDP-43 are also found in ALS patients (*83*), our data do not exclude
438 the possibility that TDP-43 NBs may become irreversible protein aggregates under extended
439 stress or diseased conditions.
440

441 **The architecture of TDP-43 NBs and the functions of the two RRMs**

442 The super-resolution 3D rendering reveals that TDP-43 NBs are ovals or cylinders in the nucleus
443 rather than perfect spheres as inferred from the 2D images. The "roundness" has been described
444 as one of the basic features for the notion that RNP granules are membraneless, intracellular
445 compartments formed by LCD-mediated phase separation. Our data suggests that substantial
446 additional forces, possibly provided by protein-protein and/or protein-RNA interactions,
447 participate in assembling and shaping RNP granules, at least for the case of TDP-43 NBs.

448 TDP-43 contains two canonical RRMs in tandem. RRM1 has a longer Loop3 region than
449 RRM2 and is thought to have a higher affinity for RNA targets (*84-85*). Although we did not
450 detect a significant difference in the binding affinity between ΔRRM1 and ΔRRM2 to total RNAs
451 in the dot-blot assay, they do show divergent sensitivities to RNA suppression in the *in vitro*
452 LLPS assays, likely because that the two RRMs have different RNA preferences (*84*). It needs to
453 be noted that the effects of RNA on ΔRRM1 and ΔRRM2 TDP-43 were compared without the
454 LCD in the *in vitro* LLPS assays. This is because the LCD presents an overwhelming
455 LLPS-driving force (*25*, *31*, *37*, *61*), whereas the *in vitro* LLPS system appears to be much less
456 suppressive than the conditions in the nucleoplasm (see below).

457 In cells, TDP-43 is diffused in the nucleus and does not form NBs spontaneously under
458 normal conditions. And, the partition of TDP-43 into phase-separated intracellular compartments
459 requires the LCD (*31*, *61*, and also see Fig. S5). Thus, ΔRRM1 and ΔRRM2 are examined
460 inclusive of the LCD in cell-based experiments in this study. ΔRRM1 lacks the RRM1-mediated
461 suppression but contains the forceful LLPS-promoting LCD, which leads to spontaneous phase
462 separation of ΔRRM1 in the nucleus. Meanwhile, since the RRM1 is also used by TDP-43 to
463 anchor itself to the core of the NBs, the phase-separated ΔRRM1 forms large, ring-like structures.
464 The seemingly conflicting effects of RRM1 – inhibiting TDP-43 phase separation under normal
465 conditions whereas pushing TDP-43 toward the core of the NBs when the LLPS occurs – may be
466 achieved by interacting with different RNAs. In contrast, since ΔRRM2 retains the main RNA
467 suppression force mediated by RRM1, it does not spontaneously phase separate in the nucleus.
468 When stressed, ΔRRM2 forms small, condensed NBs possibly because the RRM2-mediated
469 "centrifugal force" is no longer available to counteract the RRM1-mediated "centripetal force".
470 Together, we propose a "push-and-pull" model for the opposing effects of the two RRMs in
471 maintaining the "core-shell" architecture of TDP-43 NBs.
472

473 **The role of RNAs in regulating TDP-43 LDs and NBs**

474 RNA can either promote or suppress the assembly of RNP granules depending on the
475 concentrations and the types of the RNA (15, 16, *25*, *26*). In addition, the ALS/FTD-related
476 C9ORF72 repeat RNA promotes phase transition and assembly of RNP granules in cells (*86*). In
477 this study, we show that tRNA suppresses TDP-43 LLPS, similar to the effect on FUS (*50*);
478 however, tRNA was previously shown to enhance Tau LLPS (*87*). Thus, even for the same RNA,
479 its role may vary depending on the protein that it interacts with.

480 lncRNAs are thought to provide the scaffold for the assembly of paraspeckles (*64*, *65*, *67*)
481 and nuclear stress bodies (*88*, *89*). In particular, the paraspeckle lncRNA *NEAT1* are increased
482 in patients and/or animal models of several neurodegenerative diseases including ALS (*18*),
483 Alzheimer's disease (*90*), Parkinson's disease (*91*), Huntington's disease (*92*), and multiple

484 sclerosis (*93*). In this study, we find that *NEAT1* lncRNA is substantially upregulated in stressed
485 neurons and TDP-43 NBs are partially colocalized with paraspeckles, cohering with the similar
486 observations in the spinal motor neurons of early ALS patients (*18*). Further *in vitro* experiments
487 indicate that *NEAT1* RNA not only promotes TDP-43 LLPS, but also antagonizes the generally
488 "suppressive" environment modeled using tRNA. Thus, stress-induced upregulation of *NEAT1*
489 may provide nucleation scaffolds to concentrate TDP-43 and other NB proteins, which overturns
490 the suppressive environment in the nucleoplasm, leading to the emergence of TDP-43 NBs. It is
491 worth noting that lncRNAs are potential targets of TDP-43 (*94-96*), implying complicated
492 cross-regulation between TDP-43 and *NEAT1* in this cellular stress response mechanism.
493

494 **The D169G mutation and the relevance of TDP-43 NBs in ALS pathogenesis**

495 More than 30 disease-causing mutations have been identified in the gene encoding TDP-43, of
496 which most are in the LCD and the adjacent regions (*5*, *97*). D169G is the only known
497 ALS-causing mutation within the RRM of TDP-43 (*4*) and its pathogenic mechanism has been
498 elusive. Initially, it was presumed to abrogate RNA binding due to its location within the RRM (*4*).
499 However, subsequent work indicates that the binding affinity of D169G to RNA or DNA is not
500 decreased (*85*). And, although TDP-43^{D169G} exhibits slightly increased thermal stability and may
501 be more susceptible to proteolytic cleavage (*70*, *71*), it does not engender aberrant
502 oligomerization but rather increases the resistance of TDP-43 to aggregation (*70*). Further, the
503 D169G mutation does not affect TDP-43 subcellular distribution or SG recruitment (*68*, *69*; also
504 see Fig. 7). The only reported cellular alteration by D169G is that it reduces polyubiquitination
505 and co-aggregation of TDP-43 with Ubiquilin 1 (98). However, given the long-standing notion that
506 ubiquitinated cytoplasmic inclusions containing TDP-43 is a hallmark and major cause of the
507 disease (*6*, *10*, *11*), it is difficult to understand how decreased ubiquitination and aggregation of
508 TDP-43^{D169G} leads to disease pathogenesis.

509 In this study, we discover that TDP-43^{D169G} has a striking and specific defect in the formation
510 of stress-induced TDP-43 NBs but not SGs. D169G is thought to cause a small local

511 conformational change in the Turn6 of the β-sheets within the RRM1 of TDP-43 (*70*, *71*), but
512 does not reduce the overall binding affinity of TDP-43 to nucleic acids (*85*). Indeed, we find that
513 the suppression of TDP-43 LLPS by total RNAs is unaffected by D169G, whereas the induction
514 of TDP-43 LLPS by *NEAT1* is dramatically diminished. Together with the cytoprotective role of
515 TDP-43 NBs, D169G provides a paradigm for compromise of TDP-43 NBs involved in ALS
516 pathogenesis. Given that cytoplasmic mislocalization and nuclear depletion of TDP-43 are
517 common in diseased neurons, it is likely that loss of the TDP-43 NB-mediated stress-mitigating
518 function may also underlie other cases of ALS and related diseases.

519 **REFERENCES AND NOTES**

520 1. J. P. Taylor, R. H. Brown, Jr., D. W. Cleveland, Decoding ALS: from genes to mechanism.
521 *Nature* **539**, 197-206 (2016).

522 2. M. A. van Es *et al*., Amyotrophic lateral sclerosis. *The Lancet* **390**, 2084-2098 (2017).

523 3. M. Neumann *et al*., Ubiquitinated TDP-43 in frontotemporal lobar degeneration and
524 amyotrophic lateral sclerosis. *Science* **314**, 130-133 (2006).

525 4. E. Kabashi *et al*., TARDBP mutations in individuals with sporadic and familial amyotrophic
526 lateral sclerosis. *Nat Genet* **40**, 572-574 (2008).

527 5. E. B. Lee, V. M. Lee, J. Q. Trojanowski, Gains or losses: molecular mechanisms of
528 TDP43-mediated neurodegeneration. *Nat Rev Neurosci* **13**, 38-50 (2011).

529 6. A. Jovicic, J. W. Paul, 3rd, A. D. Gitler, Nuclear transport dysfunction: a common theme in
530 amyotrophic lateral sclerosis and frontotemporal dementia. *J Neurochem* **138 Suppl 1**,
531 134-144 (2016).

532 7. A. Ratti, E. Buratti, Physiological functions and pathobiology of TDP-43 and FUS/TLS
533 proteins. *J Neurochem* **138 Suppl 1**, 95-111 (2016).

534 8. H. Ederle, D. Dormann, TDP-43 and FUS en route from the nucleus to the cytoplasm. *FEBS*
535 *Letters* **591**, 1489-1507 (2017).

536 9. B. Fahrenkrog, A. Harel, Perturbations in Traffic: Aberrant Nucleocytoplasmic Transport at
537 the Heart of Neurodegeneration. *Cells* **7**, 232 (2018).

538 10. M. Zhao, J. R. Kim, R. van Bruggen, J. Park, RNA-Binding Proteins in Amyotrophic Lateral
539 Sclerosis. *Mol Cells* **41**, 818-829 (2018).

540 11. Y. R. Li, O. D. King, J. Shorter, A. D. Gitler, Stress granules as crucibles of ALS
541 pathogenesis. *J Cell Biol* **201**, 361-372 (2013).

542 12. M. Ramaswami, J. P. Taylor, R. Parker, Altered ribostasis: RNA-protein granules in
543 degenerative disorders. *Cell* **154**, 727-736 (2013).

544 13. T. Murakami *et al*., ALS/FTD Mutation-Induced Phase Transition of FUS Liquid Droplets and
545 Reversible Hydrogels into Irreversible Hydrogels Impairs RNP Granule Function. *Neuron* **88**,
546 678-690 (2015).

547 14. A. Patel *et al*., A Liquid-to-Solid Phase Transition of the ALS Protein FUS Accelerated by
548 Disease Mutation. *Cell* **162**, 1066-1077 (2015).

549 15. D. Stanek, A. H. Fox, Nuclear bodies: news insights into structure and function. *Curr Opin*
550 *Cell Biol* **46**, 94-101 (2017).

551 16. M. Wegener, M. Muller-McNicoll, Nuclear retention of mRNAs - quality control, gene
552 regulation and human disease. *Semin Cell Dev Biol* **79**, 131-142 (2018).

553 17. E. B. Dammer *et al*., Coaggregation of RNA-binding proteins in a model of TDP-43
554 proteinopathy with selective RGG motif methylation and a role for RRM1 ubiquitination.
555 *PLoS One* **7**, e38658 (2012).

556 18. Y. Nishimoto *et al*., The long non-coding RNA nuclear-enriched abundant transcript 1_2
557 induces paraspeckle formation in the motor neuron during the early phase of amyotrophic
558 lateral sclerosis. *Mol Brain* **6**, 31 (2013).

559 19. J. A. West *et al*., Structural, super-resolution microscopy analysis of paraspeckle nuclear
560 body organization. *J Cell Biol* **214**, 817-830 (2016).

561 20. T. Ishihara *et al*., Decreased number of Gemini of coiled bodies and U12 snRNA level in
562 amyotrophic lateral sclerosis. *Hum Mol Genet* **22**, 4136-4147 (2013).

563 21. M. Udan-Johns *et al*., Prion-like nuclear aggregation of TDP-43 during heat shock is
564 regulated by HSP40/70 chaperones. *Hum Mol Genet* **23**, 157-170 (2014).

565 22. S. Lee *et al*., Identification of a subnuclear body involved in sequence-specific cytokine RNA
566 processing. *Nat Commun* **6**, 5791 (2015).

567 23. L. Lo Piccolo *et al*., Loss of ISWI Function in Drosophila Nuclear Bodies Drives Cytoplasmic
568 Redistribution of Drosophila TDP-43. *Int J Mol Sci* **19**, 1082 (2018).

569 24. H. An *et al*., ALS-linked FUS mutations confer loss and gain of function in the nucleus by
570 promoting excessive formation of dysfunctional paraspeckles. *Acta Neuropathol Commun* **7**,
571 7 (2019).

572 25. Y. Lin, D. S. Protter, M. K. Rosen, R. Parker, Formation and Maturation of Phase-Separated
573 Liquid Droplets by RNA-Binding Proteins. *Mol Cell* **60**, 208-219 (2015).

574 26. M. Feric *et al*., Coexisting Liquid Phases Underlie Nucleolar Subcompartments. *Cell* **165**,
575 1686-1697 (2016).

576 27. S. F. Banani, H. O. Lee, A. A. Hyman, M. K. Rosen, Biomolecular condensates: organizers
577 of cellular biochemistry. *Nat Rev Mol Cell Biol* **18**, 285-298 (2017).

578 28. V. N. Uversky, Intrinsically disordered proteins in overcrowded milieu: Membrane-less
579 organelles, phase separation, and intrinsic disorder. *Curr Opin Struct Biol* **44**, 18-30 (2017).

580 29. S. Nakagawa, T. Yamazaki, T. Hirose, Molecular dissection of nuclear paraspeckles:
581 towards understanding the emerging world of the RNP milieu. *Open Biol* **8**, pii: 180150
582 (2018).

583 30. A. A. Hyman, C. A. Weber, F. Julicher, Liquid-liquid phase separation in biology. *Annu Rev*
584 *Cell Dev Biol* **30**, 39-58 (2014).

585 31. A. Molliex *et al*., Phase separation by low complexity domains promotes stress granule
586 assembly and drives pathological fibrillization. *Cell* **163**, 123-133 (2015).

587 32. H. B. Schmidt, R. Rohatgi, In Vivo Formation of Vacuolated Multi-phase Compartments

588 Lacking Membranes. *Cell Rep* **16**, 1228-1236 (2016).

589 33. I. R. Mackenzie *et al*., TIA1 Mutations in Amyotrophic Lateral Sclerosis and Frontotemporal
590 Dementia Promote Phase Separation and Alter Stress Granule Dynamics. *Neuron* **95**,
591 808-816.e809 (2017).

592 34. V. H. Ryan *et al*., Mechanistic View of hnRNPA2 Low-Complexity Domain Structure,
593 Interactions, and Phase Separation Altered by Mutation and Arginine Methylation. *Molecular*
594 *Cell* **69**, 465-479.e467 (2018).

595 35. L. Wang, J. Kang, L. Lim, Y. Wei, J. Song, TDP-43 NTD can be induced while CTD is
596 significantly enhanced by ssDNA to undergo liquid-liquid phase separation. *Biochem*
597 *Biophys Res Commun* **499**, 189-195 (2018).

598 36. S. Hennig *et al*., Prion-like domains in RNA binding proteins are essential for building
599 subnuclear paraspeckles. *J Cell Biol* **210**, 529-539 (2015).

600 37. S. Xiang *et al*., The LC Domain of hnRNPA2 Adopts Similar Conformations in Hydrogel
601 Polymers, Liquid-like Droplets, and Nuclei. *Cell* **163**, 829-839 (2015).

602 38. D. T. Murray *et al*., Structure of FUS Protein Fibrils and Its Relevance to Self-Assembly and
603 Phase Separation of Low-Complexity Domains. *Cell* **171**, 615-627 e616 (2017).

604 39. O. A. Brady, P. Meng, Y. Zheng, Y. Mao, F. Hu, Regulation of TDP-43 aggregation by
605 phosphorylation and p62/SQSTM1. *J Neurochem* **116**, 248-259 (2011).

606 40. T. J. Cohen *et al*., An acetylation switch controls TDP-43 function and aggregation
607 propensity. *Nat Commun* **6**, 5845 (2015).

608 41. W. Li *et al*., Heat Shock-induced Phosphorylation of TAR DNA-binding Protein 43 (TDP-43)
609 by MAPK/ERK Kinase Regulates TDP-43 Function. *J Biol Chem* **292**, 5089-5100 (2017).

610 42. M. Hofweber *et al*., Phase Separation of FUS Is Suppressed by Its Nuclear Import Receptor
611 and Arginine Methylation. *Cell* **173**, 706-719.e713 (2018).

612 43. F. Luo *et al*., Atomic structures of FUS LC domain segments reveal bases for reversible
613 amyloid fibril formation. *Nat Struct Mol Biol* **25**, 341-346 (2018).

614 44. L. McGurk *et al*., Poly(ADP-Ribose) Prevents Pathological Phase Separation of TDP-43 by
615 Promoting Liquid Demixing and Stress Granule Localization. Molecular *Cell* **71**,
616 703-717.e709 (2018).

617 45. S. Qamar *et al*., FUS Phase Separation Is Modulated by a Molecular Chaperone and
618 Methylation of Arginine Cation-pi Interactions. *Cell* **173**, 720-734 e715 (2018).

619 46. Y. Duan *et al*., PARylation regulates stress granule dynamics, phase separation, and
620 neurotoxicity of disease-related RNA-binding proteins. *Cell Res* **29**, 233-247 (2019).

621 47. D. Dominguez *et al*., Sequence, Structure, and Context Preferences of Human RNA Binding
622 Proteins. *Mol Cell* **70**, 854-867 e859 (2018).

623 48. S. Namkoong, A. Ho, Y. M. Woo, H. Kwak, J. H. Lee, Systematic Characterization of
624 Stress-Induced RNA Granulation. *Mol Cell* **70**, 175-187 e178 (2018).

625 49. S. P. Shevtsov, M. Dundr, Nucleation of nuclear bodies by RNA. *Nat Cell Biol* **13**, 167-173
626 (2011).

627 50. S. Maharana *et al*., RNA buffers the phase separation behavior of prion-like RNA binding
628 proteins. *Science* **360**, 918-921 (2018).

629 51. J. R. Mann *et al*., RNA Binding Antagonizes Neurotoxic Phase Transitions of TDP-43.
630 *Neuron* **102**, 1-18 (2019).

631 52. L. Bernstam, J. Nriagu, Molecular aspects of arsenic stress. *J Toxicol Environ Health B Crit*
632 *Rev* **3**, 293-322 (2000).

633 53. L. A. Kominek, Cycloheximide Production by Streptomyces griseus Control Mechanisms of
634 Cycloheximide Biosynthesis. *Antimicrob Agents Chemother* **7**, 856-860 (1975).

635 54. F. Frottin *et al*., The nucleolus functions as a phase-separated protein quality control
636 compartment. *Science* **365**, 342-347 (2019).

637 55. D. Glick, S. Barth, K. F. Macleod, Autophagy: cellular and molecular mechanisms. *J Pathol*
638 **221**, 3-12 (2010).

639 56. S. J. Barmada *et al*., Autophagy induction enhances TDP43 turnover and survival in
640 neuronal ALS models. *Nature Chemical Biology* **10**, 677-685 (2014).

641 57. A. H. Brand, N. Perrimon, Targeted gene expression as a means of altering cell fates and
642 generating dominant phenotypes. *Development* **118**, 401-415 (1993).

643 58. A. C. Groth, M. Fish, R. Nusse, M. P. Calos, Construction of transgenic Drosophila by using
644 the site-specific integrase from phage PhiC31. *Genetics* **166**, 1775-1782 (2003).

645 59. J. R. Bateman, A. M. Lee, C. T. Wu, Site-specific transformation of Drosophila via phiC31
646 integrase-mediated cassette exchange. *Genetics* **173**, 769-777 (2006).

647 60. J. Bischof, R. K. Maeda, M. Hediger, F. Karch, K. Basler, An optimized transgenesis system
648 for Drosophila using germ-line-specific phiC31 integrases. *Proc Natl Acad Sci U S A* **104**,
649 3312-3317 (2007).

650 61. A. E. Conicella, G. H. Zerze, J. Mittal, N. L. Fawzi, ALS Mutations Disrupt Phase Separation
651 Mediated by alpha-Helical Structure in the TDP-43 Low-Complexity C-Terminal Domain.
652 *Structure* **24**, 1537-1549 (2016).

653 62. L. Guo, J. Shorter, It's Raining Liquids: RNA Tunes Viscoelasticity and Dynamics of
654 Membraneless Organelles. *Mol Cell* **60**, 189-192 (2015).

655 63. J. R. Tollervey *et al*., Characterizing the RNA targets and position-dependent splicing
656 regulation by TDP-43. *Nat Neurosci* **14**, 452-458 (2011).

657 64. C. M. Clemson *et al*., An architectural role for a nuclear noncoding RNA: NEAT1 RNA is

658 essential for the structure of paraspeckles. *Mol Cell* **33**, 717-726 (2009).

659 65. L. L. Chen, G. G. Carmichael, Altered nuclear retention of mRNAs containing inverted
660 repeats in human embryonic stem cells: functional role of a nuclear noncoding RNA. *Mol*
661 *Cell* **35**, 467-478 (2009).

662 66. Y. T. Sasaki, T. Ideue, M. Sano, T. Mituyama, T. Hirose, MENepsilon/beta noncoding RNAs
663 are essential for structural integrity of nuclear paraspeckles. *Proc Natl Acad Sci U S A* **106**,
664 2525-2530 (2009).

665 67. T. Yamazaki *et al*., Functional Domains of NEAT1 Architectural lncRNA Induce Paraspeckle
666 Assembly through Phase Separation. *Molecular Cell* **70**, 1038-1053.e1037 (2018).

667 68. K. K. McDonald *et al*., TAR DNA-binding protein 43 (TDP-43) regulates stress granule
668 dynamics via differential regulation of G3BP and TIA-1. *Hum Mol Genet* **20**, 1400-1410
669 (2011).

670 69. E. Bentmann *et al*., Requirements for stress granule recruitment of fused in sarcoma (FUS)
671 and TAR DNA-binding protein of 43 kDa (TDP-43). *J Biol Chem* **287**, 23079-23094 (2012).

672 70. J. A. Austin *et al*., Disease causing mutants of TDP-43 nucleic acid binding domains are
673 resistant to aggregation and have increased stability and half-life. *Proc Natl Acad Sci U S A*
674 **111**, 4309-4314 (2014).

675 71. C. H. Chiang *et al*., Structural analysis of disease-related TDP-43 D169G mutation: linking
676 enhanced stability and caspase cleavage efficiency to protein accumulation. *Sci Rep* **6**,
677 21581 (2016).

678 72. Y. C. Liu, P. M. Chiang, K. J. Tsai, Disease animal models of TDP-43 proteinopathy and
679 their pre-clinical applications. *Int J Mol Sci* **14**, 20079-20111 (2013).

680 73. A. H. Fox *et al*., Paraspeckles: A Novel Nuclear Domain. *Current Biology* **12**, 13-25 (2002)

681 74. K. V. Prasanth *et al*., Regulating gene expression through RNA nuclear retention. *Cell* **123**,
682 249-263 (2005).

683 75. T. Naganuma *et al*., Alternative 3'-end processing of long noncoding RNA initiates
684 construction of nuclear paraspeckles. *EMBO J* **31**, 4020-4034 (2012).

685 76. C. S. Bond, A. H. Fox, Paraspeckles: nuclear bodies built on long noncoding RNA. *J Cell*
686 *Biol* **186**, 637-644 (2009).

687 77. A. H. Fox, A. I. Lamond, Paraspeckles. *Cold Spring Harb Perspect Biol* **2**, a000687 (2010).

688 78. A. H. Fox, S. Nakagawa, T. Hirose, C. S. Bond, Paraspeckles: Where Long Noncoding RNA
689 Meets Phase Separation. *Trends Biochem Sci* **43**, 124-135 (2018).

690 79. L. Liu-Yesucevitz *et al*., Tar DNA binding protein-43 (TDP-43) associates with stress
691 granules: analysis of cultured cells and pathological brain tissue. *PLoS One* **5**, e13250
692 (2010).

693 80. J. K. Bose, I. F. Wang, L. Hung, W. Y. Tarn, C. K. Shen, TDP-43 overexpression enhances
694 exon 7 inclusion during the survival of motor neuron pre-mRNA splicing. *J Biol Chem* **283**,
695 28852-28859 (2008).

696 81. T. W. Han *et al*., Cell-free formation of RNA granules: bound RNAs identify features and
697 components of cellular assemblies. *Cell* **149**, 768-779 (2012).

698 82. J. Seo *et al*., Oxidative Stress Triggers Body-Wide Skipping of Multiple Exons of the Spinal
699 Muscular Atrophy Gene. *PLoS One* **11**, e0154390 (2016).

700 83. M. S. Forman, J. Q. Trojanowski, V. M. Lee, TDP-43: a novel neurodegenerative
701 proteinopathy. *Curr Opin Neurobiol* **17**, 548-555 (2007).

702 84. E. Buratti, F. E. Baralle, Characterization and functional implications of the RNA binding
703 properties of nuclear factor TDP-43, a novel splicing regulator of CFTR exon 9. *J Biol Chem*
704 **276**, 36337-36343 (2001).

705 85. P. H. Kuo, C. H. Chiang, Y. T. Wang, L. G. Doudeva, H. S. Yuan, The crystal structure of
706 TDP-43 RRM1-DNA complex reveals the specific recognition for UG- and TG-rich nucleic
707 acids. *Nucleic Acids Res* **42**, 4712-4722 (2014).

708 86. M. M. Fay, P. J. Anderson, P. Ivanov, ALS/FTD-Associated C9ORF72 Repeat RNA
709 Promotes Phase Transitions In Vitro and in Cells. *Cell Rep* **21**, 3573-3584 (2017).

710 87. T. Ukmar-Godec *et al*., Lysine/RNA-interactions drive and regulate biomolecular
711 condensation. *Nat Commun* **10**, 2909 (2019).

712 88. C. Jolly et al., Stress-induced transcription of satellite III repeats. *J Cell Biol* **164**, 25-33
713 (2004).

714 89. R. Valgardsdottir et al., Structural and Functional Characterization of Noncoding Repetitive
715 RNAs Transcribed in Stressed Human Cells. *Molecular Biology of the Cell* **16**, 2597-2604
716 (2005).

717 90. N. Puthiyedth, C. Riveros, R. Berretta, P. Moscato, Identification of Differentially Expressed
718 Genes through Integrated Study of Alzheimer's Disease Affected Brain Regions. *PLoS One*
719 **11**, e0152342 (2016).

720 91. E. Mariani *et al*., Meta-Analysis of Parkinson's Disease Transcriptome Data Using TRAM
721 Software: Whole Substantia Nigra Tissue and Single Dopamine Neuron Differential Gene
722 Expression. *PLoS One* **11**, e0161567 (2016).

723 92. C. Cheng *et al*., The long non-coding RNA NEAT1 is elevated in polyglutamine repeat
724 expansion diseases and protects from disease gene-dependent toxicities. *Hum Mol Genet*
725 **27**, 4303-4314 (2018).

726 93. L. Schirmer *et al*., Neuronal vulnerability and multilineage diversity in multiple sclerosis.
727 *Nature* [Epub ahead of print] (2019).

728 94. M. Polymenidou *et al*., Long pre-mRNA depletion and RNA missplicing contribute to

729 neuronal vulnerability from loss of TDP-43. *Nat Neurosci* **14**, 459-468 (2011).

730 95. C. Y. Chung *et al*., Aberrant activation of non-coding RNA targets of transcriptional
731 elongation complexes contributes to TDP-43 toxicity. *Nat Commun* **9**, 4406 (2018).

732 96. M. Modic *et al*., Cross-Regulation between TDP-43 and Paraspeckles Promotes
733 Pluripotency-Differentiation Transition. *Mol Cell* **74**, 951-965 e913 (2019).

734 97. A. S. Chen-Plotkin, V. M. Lee, J. Q. Trojanowski, TAR DNA-binding protein 43 in
735 neurodegenerative disease. *Nat Rev Neurol* **6**, 211-220 (2010).

736 98. S. H. Kim *et al*., Potentiation of amyotrophic lateral sclerosis (ALS)-associated TDP-43
737 aggregation by the proteasome-targeting factor, ubiquilin 1. *J Biol Chem* **284**, 8083-8092
738 (2009).

739 99. X. Sun *et al*., Distinct multilevel misregulations of Parkin and PINK1 revealed in cell and
740 animal models of TDP-43 proteinopathy. *Cell Death Dis* **9**, 953 (2018).

741 100. X. Cao *et al*., In vivo imaging reveals mitophagy independence in the maintenance of axonal
742 mitochondria during normal aging. *Aging Cell* **16**, 1180-1190 (2017).

743 101. M. H. M. Koken *et al*., The t(15;17) translocation alters a nuclear body in a retinoic
744 acid-reversible fashion. *The EMBO Journal* **13**, 1073-1083 (1994).

745 102. N. Santama *et al*., Characterization of hCINAP, a novel coilin-interacting protein encoded by
746 a transcript from the transcription factor TAFIID32 locus. *J Biol Chem* **280**, 36429-36441
747 (2005).

748 103. X-D. Fu, T. Maniatis, Factor required for mammalian spliceosome assembly is localized to
749 discrete regions in the nucleus. *Nature* **343**, 437–444 (1990).

ACKNOWLEDGMENTS

We thank the BDSC for providing the fly strains, the SIBCB *Drosophila* Center for the fly embryo injection services, L. Pan, J. Zhou, and Z. Zhang for the cloning vectors and plasmids, Z. Zhang for help in the pulse-chase assay, S. Qiu for technical supports, J. Yuan, A. Li and Y. Chen for critical reading of the manuscript, and the members of the Fang lab for helpful discussion. **Funding**: Supported by grants from the National Key R&D Program of China (No. 2016YFA0501902) to Y.F., the National Natural Science Foundation of China (No. 81671254 and No. 31471017) to Y.F and (No. 91853112 and No. 31470748) to C.L, and the Alzheimer's AssOCiation (AARF-16-441196) and Target ALS Springboard Fellowship to L.G. **Author contributions:** G.D., Z.M. and Y.F. conceived the research; C.W., Y.D., G.D., C.L., L.G. and Y.F. designed the experiments; C.W., Y.D. G.D., K.Z., X.D., B.Q., J.G. and S.Z. performed the experiments; C.W., Y.D., G.D., Z.M., J.G. and C.L contributed important new reagents; C.W., Y.D. G.D., and Y.F. analyzed the data and interpreted the results; C.W., Y.D., G.D. and Y.F. prepared the figures; and C.W., Y.D. G.D., and Y.F. wrote the paper. All authors read and approved the final manuscript. **Competing interests:** None. **Data and materials availability:** All data are available in the manuscript or the supplementary materials.

SUPPLEMENTARY INFORMATION

Online Methods

Figures S1-S7

Movies S1-S2

References (99-103)

772 **FIGURES AND FIGURE LEGENDS**

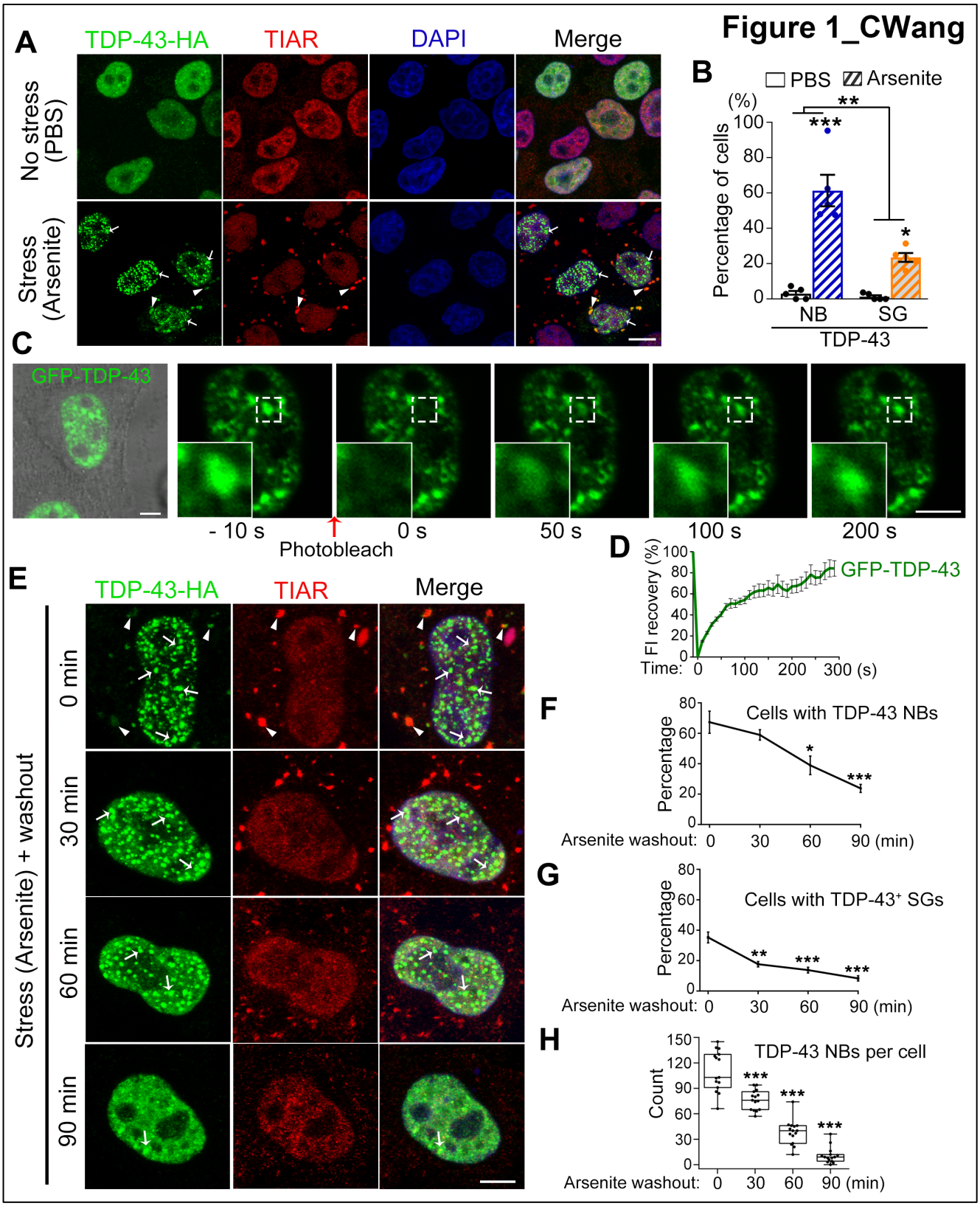

773 **Figure 1. TDP-43 forms reversible, dynamic NBs in response to arsenic stress.**

774 (**A**) Representative confocal images of HeLa cells in the absence (PBS) or presence of arsenite
775 (250 μM, 30 min) forming TDP-43 NBs (arrows) and TDP-43$^+$ SGs (arrowheads) (also see Movie
776 S1). All cells are transfected with TDP-43-HA (anti-HA) and stained for SGs with anti-TIAR;
777 merged images with DAPI staining for DNA (blue) are shown. Arrows, TDP-43 NBs; arrowheads,
778 SGs associated with TDP-43 (TDP-43$^+$ SGs). (**B**) Quantification of the percentage of cells that
779 show TDP-43 NBs or TDP-43$^+$ SGs before and after arsenite the treatment in (A). Data are
780 shown as mean ± SEM, n = ~100 cells for each group from pooled results of 3 independent
781 repeats; *$p < 0.05$, **$p < 0.01$, ***$p < 0.001$; Student's *t*-test for comparison between stress and
782 no stress within the same group, two-way ANOVA for comparison of the stress-induced changes
783 between different groups. (**C**) Representative images of the FRAP analysis of GFP-TDP-43 NBs
784 in *live* cells (also see Movie S2). (**D**) The FRAP recovery curve is quantified by averaging the
785 relative fluorescence intensity (FI) of 9 TDP-43 NBs of similar size at indicated time after
786 photobleaching. The relative FI of each TDP-43 NB prior to photobleaching is set to 100%. Time
787 0 refers to the time point right after photobleaching. (**E**) Representative images showing the
788 disappearance of TDP-43 NBs and TDP-43$^+$ SGs after arsenite washout. (**F-H**) Quantification of
789 the percentage of cells showing TDP-43 NBs (F), TDP-43$^+$ SGs (G) or the average count of
790 TDP-43 NBs per cell (H) at indicated time points after arsenite washout in (E). Mean ± SEM,
791 except for (H) box-and-whisker plots. n = ~100 cells for each group in (F-G) and ~15 cells for
792 each group in (H), pooled results from 3 independent repeats; statistic significance is determined
793 by comparing to time 0; *$p < 0.05$, **$p < 0.01$, ***$p < 0.001$; one-way ANOVA. Scale bars, 10 μm
794 in (A) and 5 μm in (C, E).
795

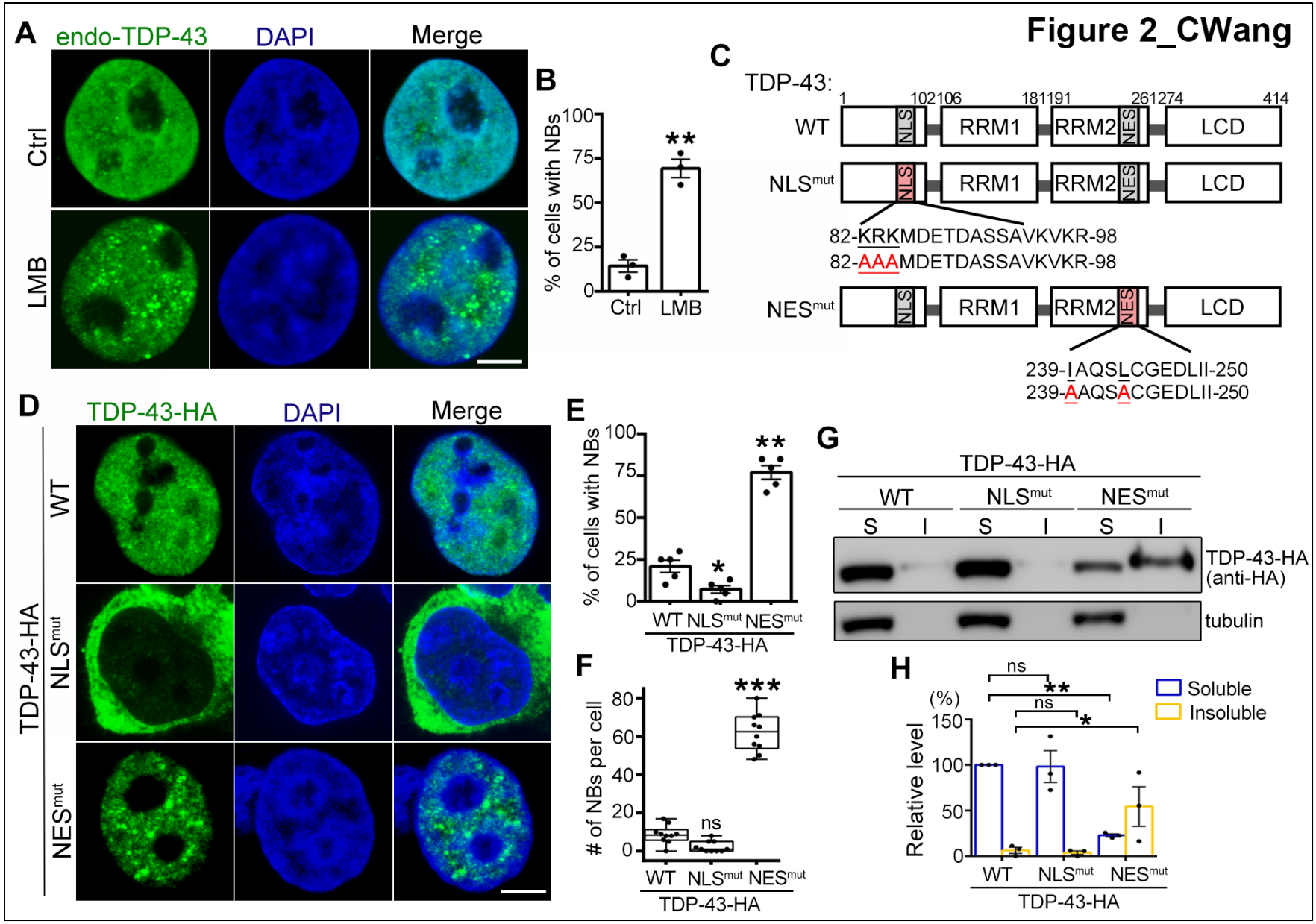
Figure 2_CWang
A
endo-TDP-43
DAPI
Merge
Ctrl
LMB
B
% of cells with NBs
100
75
50
25
0
**
Ctrl
LMB
C
TDP-43:
1
102106
181191
261274
414
WT
NLS
RRM1
RRM2
NES
LCD
NLS^mut
82-KRKMDETDASSAVKVKR-98
82-AAAMDETDASSAVKVKR-98
NES^mut
239-IAQSLCGEDLII-250
239-AAQSACGEDLII-250
D
TDP-43-HA
DAPI
Merge
TDP-43-HA
WT
NLS^mut
NES^mut
E
% of cells with NBs
100
75
50
25
0
**
*
WT
NLS^mut
NES^mut
TDP-43-HA
F
# of NBs per cell
80
60
40
20
0
***
ns
WT
NLS^mut
NES^mut
TDP-43-HA
G
TDP-43-HA
WT
NLS^mut
NES^mut
S
I
S
I
S
I
TDP-43-HA
(anti-HA)
tubulin
H
(%)
Relative level
150
100
50
0
ns
**
ns
*
Soluble
Insoluble
WT
NLS^mut
NES^mut
TDP-43-HA

796

797 **Figure 2. Inhibition of nuclear export induces TDP-43 NBs.**

798 (**A-B**) Representative images of endogenous TDP-43 (endo-TDP-43) forming NBs upon LMB
799 treatment (25 nM, 24 h). Percentage of cells showing distinct TDP-43 NBs in (A) is quantified in
800 (B). (**C**) A diagram showing the major domains of human TDP-43 and the residues mutated in
801 the localization signals. NLS, nuclear localization signal; RRM, RNA recognition motif; NES,
802 nuclear export signal; LCD, low complexity domain. (**D**) Representative images of 293T cells
803 transfected with WT, NLS^{mut} or NES^{mut} TDP-43. (**E-F**) The percentage of cells with NBs (E) and
804 the average number of NBs per cell (F) are quantified. (**G-H**) Representative Western blot
805 images (G) and quantifications (H) of WT, NLS^{mut} and NES^{mut} TDP-43 proteins in the soluble (S,
806 supernatants in RIPA) and insoluble fractions (I, pellets resuspended in 9 M of urea). Mean ±
807 SEM, except for (F) box-and-whisker plots. n >120 cells each condition in (B, E) and ~ 10 cells
808 each condition in (F) from pooled results of 3 independent repeats, n = 3 in (G-H); *$p < 0.05$, **p
809 < 0.01, ***$p < 0.001$; ns, not significant; Student's *t*-test in (B), one-way ANOVA in (E-F, H). Scale
810 bar: 5 μm.

811

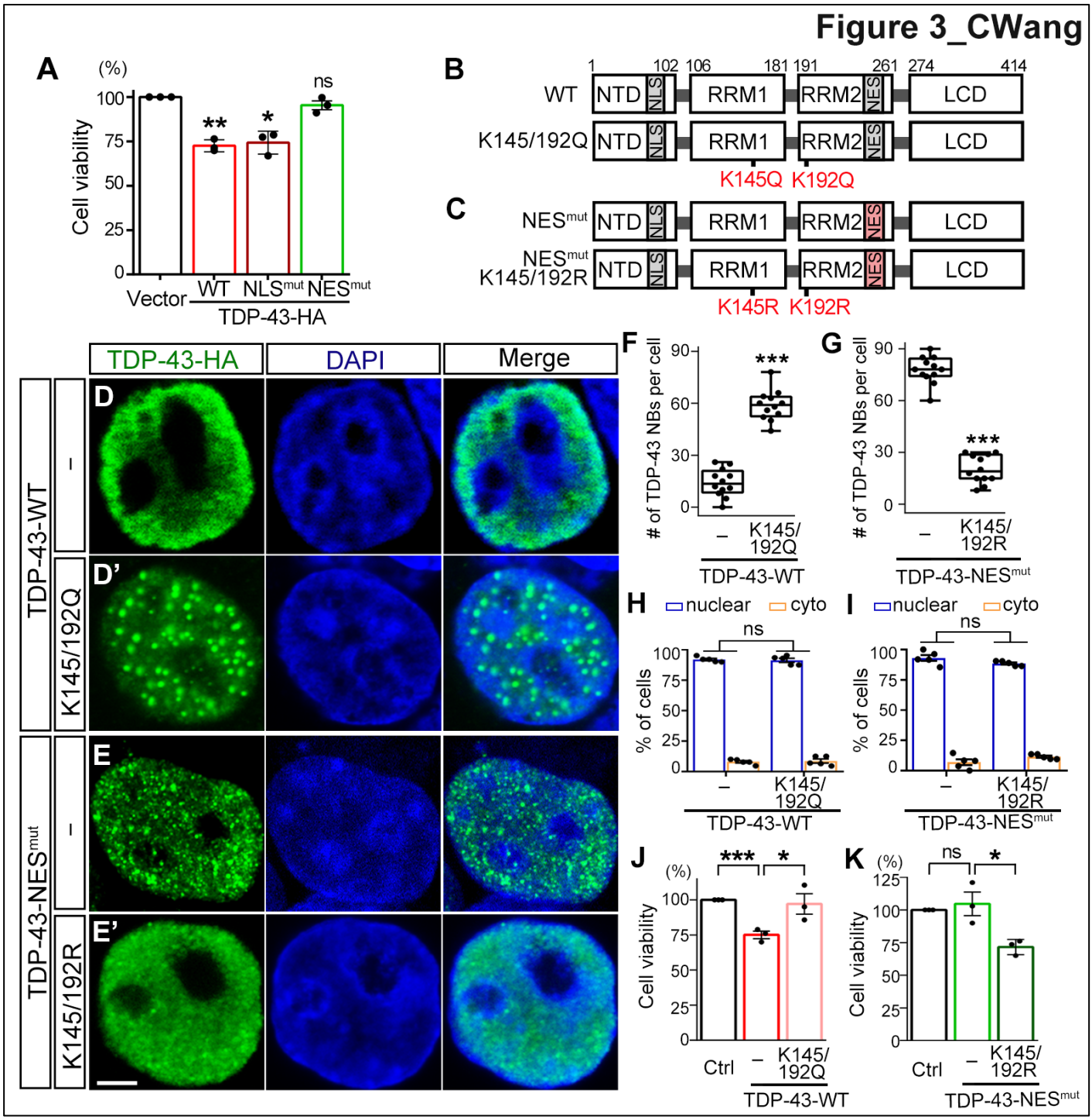
Figure 3_CWang
A
(%)
Cell viability
100
75
50
25
0
**
*
ns
Vector
WT
NLSmut
NESmut
TDP-43-HA
B
WT
K145/192Q
NTD
NLS
RRM1
RRM2
NES
LCD
1
102
106
181
191
261
274
414
K145Q K192Q
C
NESmut
NESmut K145/192R
K145R K192R
TDP-43-HA
DAPI
Merge
TDP-43-WT
TDP-43-NESmut
–
K145/192Q
K145/192R
D
D'
E
E'
F
# of TDP-43 NBs per cell
90
60
30
0
***
K145/192Q
TDP-43-WT
G
K145/192R
TDP-43-NESmut
H
nuclear
cyto
% of cells
ns
I
J
Ctrl
K
125

812

813 **Figure 3. Formation of NBs mitigates TDP-43-mediated cytotoxicity.**

814 (**A**) OE of the WT or NLS^{mut} but not NES^{mut} TDP-43 in 293T cells exhibits cytotoxicity and
815 decreases the cell viability, which is measured by the Cell Counting Kit-8 (CCK-8) assay. (**B-C**)
816 Diagrams showing the K145/192Q mutation in the WT TDP-43 and the K145/192R mutation in
817 the NES^{mut} TDP-43, respectively. (**D-E'**) Representative confocal images of the WT (D) and "WT
818 + K145/192Q" TDP-43 (D'), or the NES^{mut} (E) and "NES^{mut} + K145/192R" TDP-43 (E') in 293T
819 cells. (**F-G**) Quantifications of the average numbers of TDP-43 NBs per cell formed in each group
820 in (D-E') as indicated. (**H-I**) Percentages of cells with TDP-43 exclusively in the nucleus (nuclear)
821 or in both the nucleus and the cytoplasm (cyto) in (D-E') are quantified. (**J-K**) The viability of cells
822 expressing the WT or NES^{mut} TDP-43 with the indicated NB-promoting or NB-suppressing
823 mutation is assessed using the CCK-8 assay. Mean ± SEM, except for (F-G) box-and-whisker
824 plots; n = 3 in (A, J-K), n = ~12 cells each group in (F-G), n >100 cells per group in (H-I). *p <
825 0.05, **p < 0.01, ***p < 0.001; ns, not significant; one-way ANOVA in (A), Student's *t*-test in (F-G,
826 J-K), two-way ANOVA in (H-I). Scale bar: 5 μm.
827

828

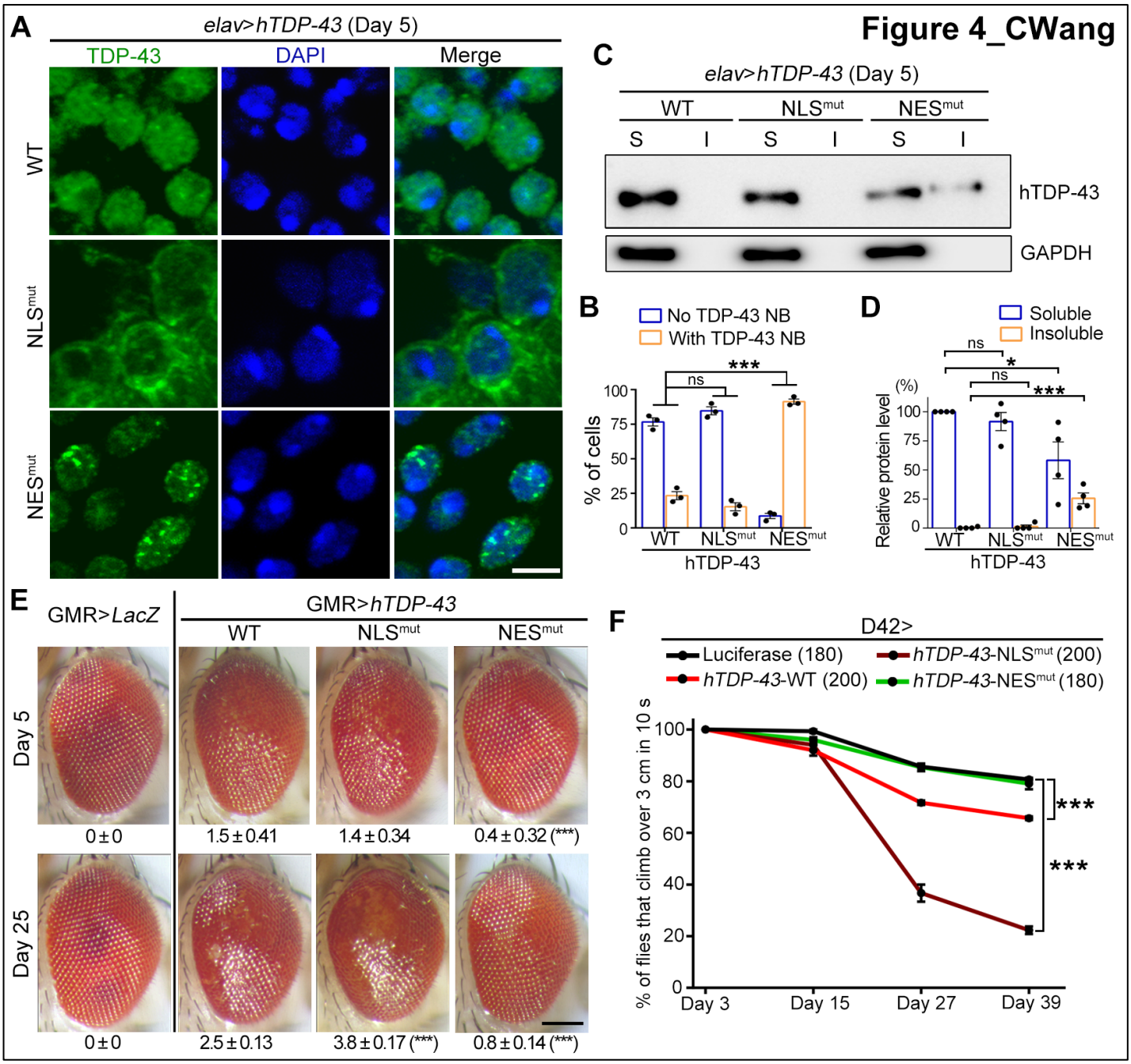
Figure 4_CWang
A
elav>hTDP-43 (Day 5)
TDP-43
DAPI
Merge
WT
NLSmut
NESmut
B
No TDP-43 NB
With TDP-43 NB
% of cells
ns
***
WT
NLSmut
NESmut
hTDP-43
C
elav>hTDP-43 (Day 5)
WT
NLSmut
NESmut
S
I
hTDP-43
GAPDH
D
Soluble
Insoluble
Relative protein level
(%)
ns
*
***
E
GMR>LacZ
GMR>hTDP-43
Day 5
Day 25
0±0
1.5±0.41
1.4±0.34
0.4±0.32 (***)
0±0
2.5±0.13
3.8±0.17 (***)
0.8±0.14 (***)
F
D42>
Luciferase (180)
hTDP-43-NLSmut (200)
hTDP-43-WT (200)
hTDP-43-NESmut (180)
% of flies that climb over 3 cm in 10 s
Day 3
Day 15
Day 27
Day 39
***
***

829

830 **Figure 4. Transgenic flies expressing WT, NLS^{mut} or NES^{mut} hTDP-43.**

831 (**A**) Representative confocal images of the fly central brain neurons (*elav*-Gal4) expressing the
832 WT or mutant *hTDP-43* as indicated. The whole-mount fly brains were dissected and
833 immunostained for hTDP-43 (green) and DAPI (blue, to show the nucleus). (**B**) The average
834 percentages of fly neurons with or without TDP-43 NBs are quantified. Mean ± SEM, n = ~100
835 neurons each group. (**C-D**) Representative image (C) and quantification (D) of Western blot
836 analysis of the WT or mutant hTDP-43 protein extracted from the fly head in RIPA-soluble (S) or
837 RIPA-insoluble (I, resuspended in 9 M of urea) fractions. All protein levels are normalized to
838 GAPDH. The relative level of soluble TDP-43-WT is set to 100%. Mean ± SEM, n = 4. (**E**)
839 Representative z-stack images of the fly eye (GMR-Gal4) expressing the WT or mutant hTDP-43
840 transgenes as indicated at Day 5 or Day 25. The average degeneration score (mean ± SEM) and
841 the statistic significance (compared to hTDP-43-WT flies) of each group are indicated at the
842 bottom. n = 8 eyes each group. (**F**) The climbing capability of the flies expressing the WT or
843 mutant hTDP-43 in motor neurons (D42-Gal4) is evaluated as percentage of flies climbing over 3
844 cm in 10 seconds. Control, UAS-*luciferase*. Mean ± SEM, the number of flies tested for each
845 genotype is shown. *$p < 0.05$, ***$p < 0.001$; ns, not significant; two-way ANOVA in (B, F),
846 one-way ANOVA in (D-E). Scale bars: 2 μm in (A) and 100 μm in (E).
847

848

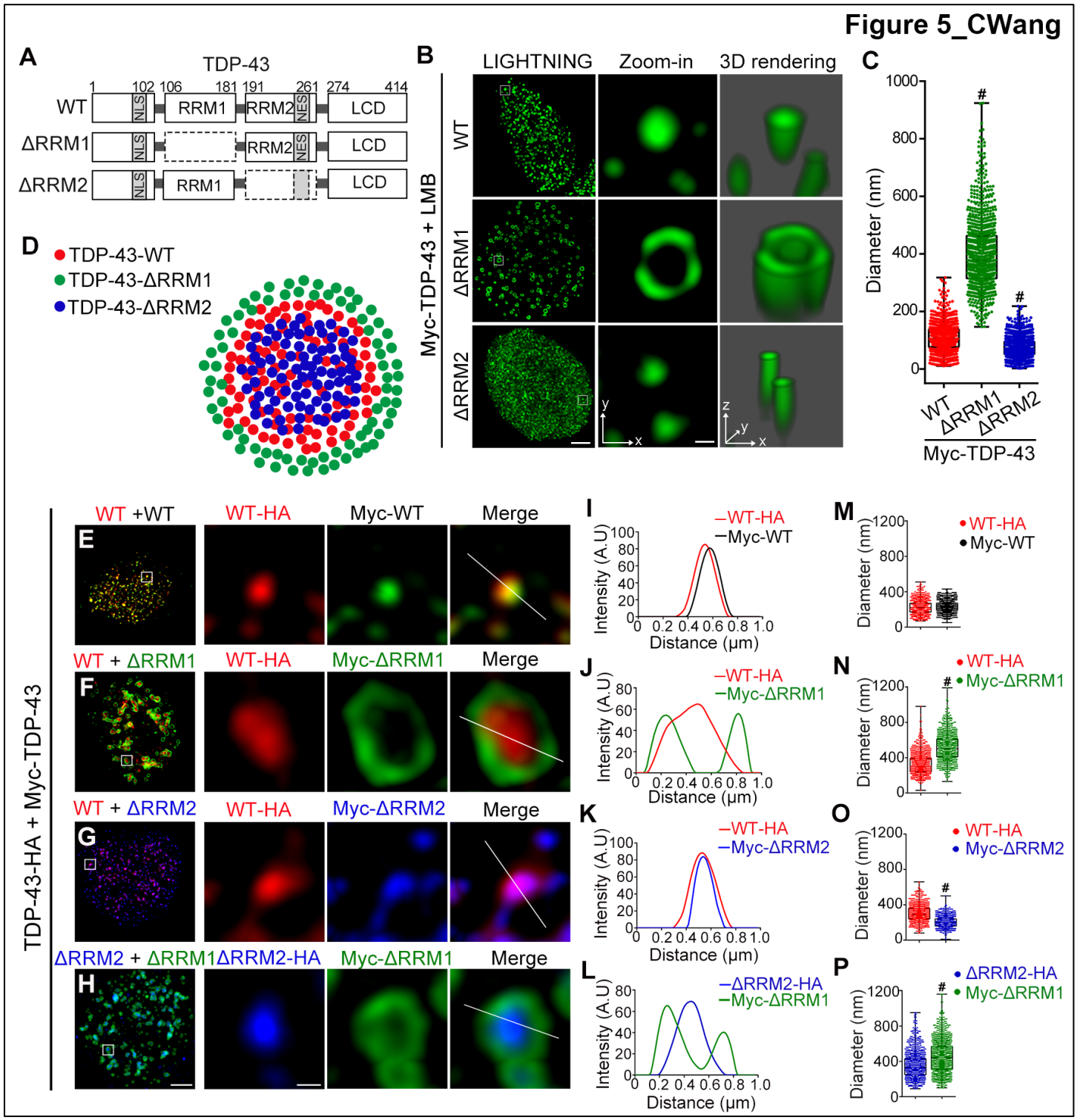
Figure 5_CWang
A
TDP-43
1 102 106 181 191 261 274 414
WT
ΔRRM1
ΔRRM2
NLS
RRM1
RRM2
NES
LCD
B
LIGHTNING
Zoom-in
3D rendering
Myc-TDP-43 + LMB
C
Diameter (nm)
Myc-TDP-43
D
TDP-43-WT
TDP-43-ΔRRM1
TDP-43-ΔRRM2
TDP-43-HA + Myc-TDP-43
WT +WT
WT-HA
Myc-WT
Merge
WT + ΔRRM1
Myc-ΔRRM1
WT + ΔRRM2
Myc-ΔRRM2
ΔRRM2 + ΔRRM1
ΔRRM2-HA
Intensity (A.U)
Distance (μm)
Myc-TDP-43

849

850 **Figure 5. The role of RRM1 and RRM2 in maintaining the architecture of TDP-43 NBs.**
851 (**A**) A diagram showing the major functional domains of WT TDP-43 and the ΔRRM1 and
852 ΔRRM2 mutants. (**B**) LIGHTNING super-resolution microscopy of 293T cells transfected with
853 Myc-TDP-43-WT, ΔRRM1 or ΔRRM2 and treated with LMB. Higher magnification images
854 (zoom-ins) and 3D renderings of the boxed areas are shown. (**C**) The average diameters of the
855 WT, ΔRRM1 and ΔRRM2 TDP-43 nuclear structures in (B) are quantified. (**D**) A schematic
856 model of the core-shell architecture of TDP-43 NBs (red) and the distinct distribution of ΔRRM1
857 (green) and ΔRRM2 (blue). (**E-H**) LIGHTNING multicolor super-resolution microscopy and higher
858 magnification images of representative LMB-induced TDP-43 NBs. Cells are co-transfected with
859 a combination of HA- or Myc-tagged WT, ΔRRM1 or ΔRRM2 TDP-43 as indicated. (**I-P**) The
860 intensity profiles (I-L) along the indicated lines and the average diameters (M-P) of TDP-43 NBs
861 in each group are shown. The box-and-whisker plots with the value of each NB measured are
862 shown. n = ~900 NBs in (C, M-P) for each group from pooled results of at least 3 independent
863 repeats; $^{\#}p < 0.0001$; one-way ANOVA in (C) and Student's *t*-test in (M-P). Scale bars: 5 μm in
864 (B), 2 μm in (E-H) and 200 nm in the zoom-ins.
865

866

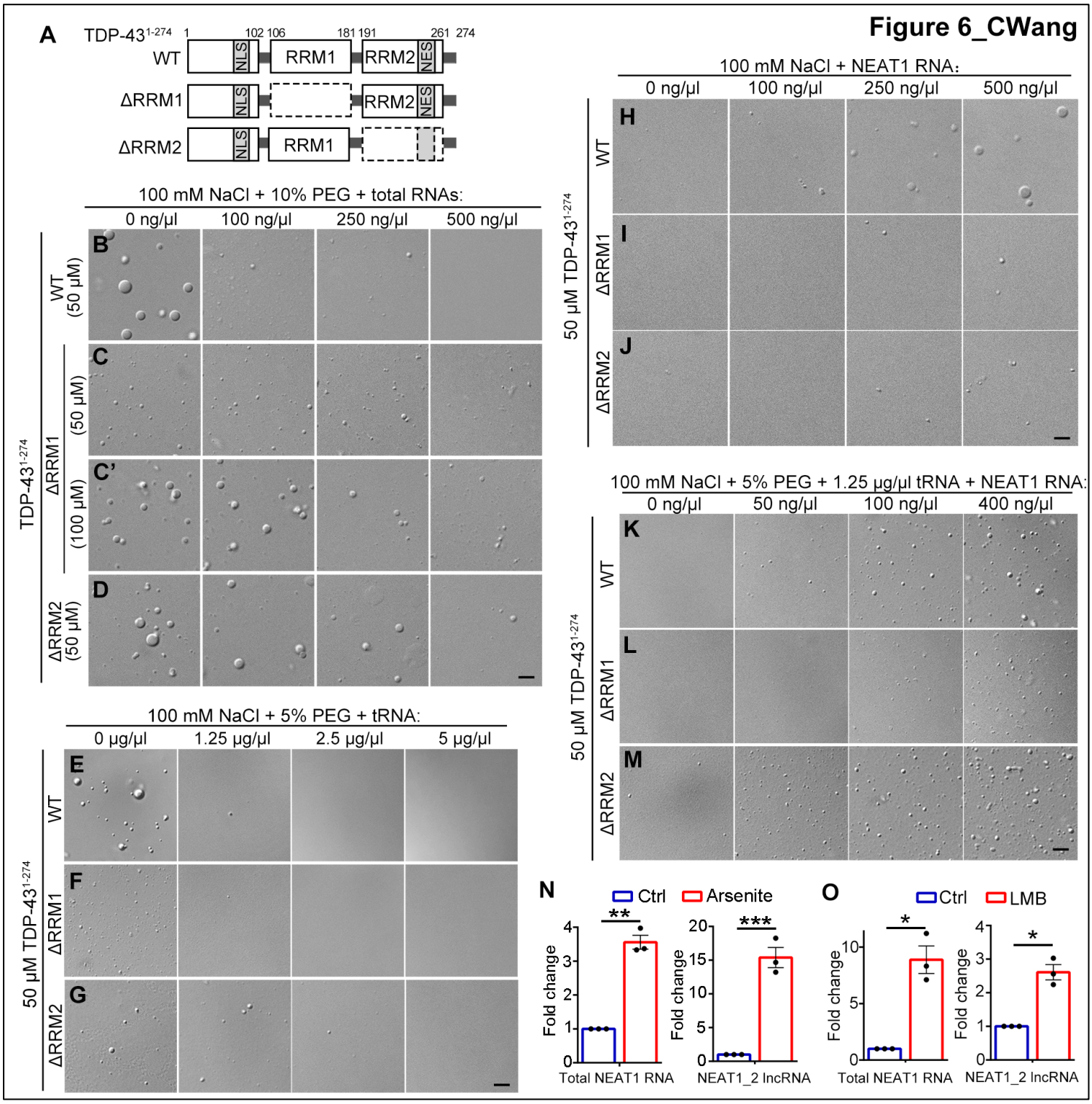
Figure 6_CWang
A
TDP-43 1-274
1
102 106
181 191
261 274
WT
ΔRRM1
ΔRRM2
NLS
RRM1
RRM2
NES
100 mM NaCl + 10% PEG + total RNAs:
0 ng/μl
100 ng/μl
250 ng/μl
500 ng/μl
TDP-43 1-274
WT (50 μM)
ΔRRM1 (50 μM)
ΔRRM1 (100 μM)
ΔRRM2 (50 μM)
B
C
C'
D
100 mM NaCl + 5% PEG + tRNA:
0 μg/μl
1.25 μg/μl
2.5 μg/μl
5 μg/μl
50 μM TDP-43 1-274
E
F
G
100 mM NaCl + NEAT1 RNA:
H
I
J
100 mM NaCl + 5% PEG + 1.25 μg/μl tRNA + NEAT1 RNA:
0 ng/μl
50 ng/μl
100 ng/μl
400 ng/μl
K
L
M
N
Ctrl
Arsenite
Fold change
Total NEAT1 RNA
NEAT1_2 lncRNA
O
LMB

867

868 **Figure 6. The effects of different RNAs on TDP-43 LLPS *in vitro*.**

869 (**A**) A diagram showing the WT, ΔRRM1 and ΔRRM2 of TDP-43$^{1-274}$. (**B-D**) The total RNA
870 extracts, (**E-G**) tRNA, and (**H-J**) lncRNA *NEAT1* are added into the *in vitro* LLPS assay of WT,
871 ΔRRM1 and ΔRRM2 TDP-43$^{1-273}$ as indicated. C', a higher concentration of ΔRRM1 is also
872 included in order to start the suppression assay with large LDs as those of WT TDP-43. (**K-M**)
873 tRNA-mediated suppression of TDP-43 LLPS can be antagonized by increasing *NEAT1* RNA
874 levels. The concentrations of NaCl, the crowding agent PEG, TDP-43 proteins and RNAs used in
875 the *in vitro* assays are as indicated. (**N-O**) Cellular stress induced by arsenite (N) or LMB (O)
876 increases *NEAT1* RNA levels in mouse primary neurons compared to the vehicle control PBS
877 and ethanol, respectively. Mean ± SEM, n = 3; *$p < 0.05$, **$p < 0.01$, ***$p < 0.001$; Student's *t*-test.
878 Scale bars: 2 μm.
879

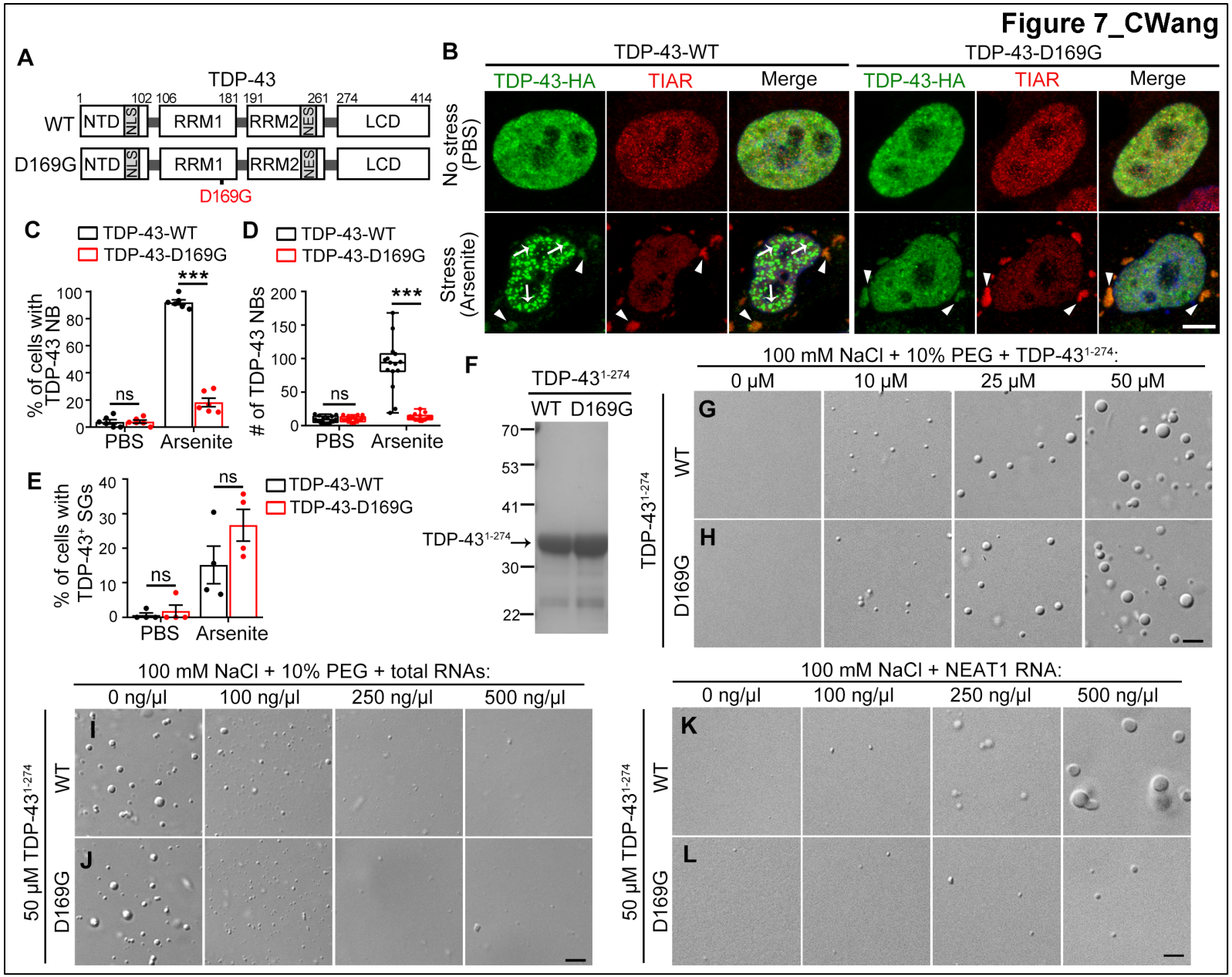
Figure 7_CWang
A
TDP-43
WT
D169G
NTD
NLS
RRM1
RRM2
NES
LCD
D169G
B
TDP-43-WT
TDP-43-D169G
TDP-43-HA
TIAR
Merge
No stress (PBS)
Stress (Arsenite)
C
TDP-43-WT
TDP-43-D169G
% of cells with TDP-43 NB
ns
***
PBS
Arsenite
D
# of TDP-43 NBs
E
% of cells with TDP-43+ SGs
F
TDP-43 1-274
WT D169G
100 mM NaCl + 10% PEG + TDP-43 1-274:
0 μM
10 μM
25 μM
50 μM
G
H
100 mM NaCl + 10% PEG + total RNAs:
0 ng/μl
100 ng/μl
250 ng/μl
500 ng/μl
I
J
50 μM TDP-43 1-274
100 mM NaCl + NEAT1 RNA:
K
L

880

881 **Figure 7. The ALS-associated D169G mutation impairs the ability of TDP-43 to form**
882 **stress-induced NBs and *NEAT1*-promoted LDs.**
883 (**A**) A diagram showing WT and D169G mutant TDP-43. (**B**) Representative confocal images of
884 HeLa cells transfected with WT or D169G TDP-43 in the absence (PBS) or presence of arsenite.
885 Green, TDP-43-HA (anti-HA); Red, anti-TIAR for SGs; Blue, DAPI staining for DNA (nucleus).
886 Arrows, TDP-43 NBs; arrowheads, TDP-43^{+} SGs. (**C-E**) The percentage of cells with TDP-43
887 NBs (C), the average count of TDP-43 NBs per cell (D) and the percentage of cells with TDP-43^{+}
888 SGs (E) in (B) are quantified. Mean ± SEM, except for (D) box-and-whisker plots; n = ~100 cells
889 for each group in (C, E) and n = ~15 cells for each group in (D) from pooled results of 3
890 independent repeats; ***p < 0.001; ns, not significant; Student's *t*-test. (**F**) Coomassie blue
891 staining confirming the purified WT and D169G TDP-43$^{1-274}$ proteins used in the *in vitro* LLPS
892 assays. (**G-H**) Both WT and D169G TDP-43 form LDs by LLPS in a dose-dependent manner.
893 (**I-J**) Suppression of the *in vitro* LLPS of WT and D169G TDP-43 by total RNA extracts. (**K-L**)
894 Promotion of TDP-43 LLPS by *NEAT1* RNA is dramatically reduced in the D169G TDP-43. The
895 concentrations of NaCl, TDP-43, PEG and RNA used in the *in vitro* assays are as indicated.
896 Scale bars: 5 μm in (B) and 2 μm in (G-L).

Supplementary Information for

Stress induces cytoprotective TDP-43 nuclear bodies through lncRNA *NEAT1*-promoted phase separation

Chen Wang, Yongjia Duan, Gang Duan, Zhiwei Ma, Kai Zhang, Xue Deng, Beituo Qian, Jinge Gu, Shuang Zhang, Lin Guo, Cong Liu, and Yanshan Fang

Correspondence to: fangys@sioc.ac.cn

This PDF file includes:

Online Methods

Figure S1 to S7

Captions for Movies S1 to S2

Other Supplementary Data for this manuscript include the following:

Movies S1 to S2

Online Methods

Plasmids and constructs

The pcDNA3.1-TDP-43-HA and pCMV-myc-TDP-43 plasmids were as previously described (*99*) and used as the templates to generate the following plasmids. The pcDNA3.1-TDP-43-NES^{mut}, NLS^{mut}, D169G and M337V-HA plasmids were generated by site-directed mutagenesis using the Fast Mutagenesis Kit II (Vazyme). The pcDNA3.1-TDP-43-K145/192Q-HA and pcDNA3.1-TDP-43-NES^{mut}-K145/192R-HA plasmids were generated by site-directed mutagenesis using the Fast Mutagenesis Kit MultiS (Vazyme). The pCMV-myc-TDP-43$^{1-274}$ pCMV-myc-TDP-43-ΔRRM1, and pCMV-myc-TDP-43-ΔRRM2 plasmids were generated by PCR using the pCMV-myc-TDP-43 plasmid as a template. To generate the pCAG-GFP-TDP-43 plasmid, the GFP coding sequence was amplified from pcDNA3.1-GFP-AXR3 (a gift from Dr. Z. Zhang) by PCR and then subcloned into a pCAG-hTDP-43 plasmid (*99*) using the ClonExpress MultiS One Step Cloning Kit (Vazyme).

For lentivirus infection of mouse primary neurons, the pLenti-hSyn-TDP-43-HA plasmid was generated by PCR using the pcDNA3.1-TDP-43-HA as a template and sub-cloned into the pLenti-hSyn vector (a gift from Dr. Y. Chen).

For generation of transgenic fly lines, the WT and mutant UAS-hTDP-43 constructs were generated by PCR using the above plasmids as a template and sub-cloned into the pBID-UASC-6*Myc vector (100) between the KpnI and ApaI sites.

For *Escherichia coli* (*E. coli*) expression, the pET28a-6×His-sumo-TDP-43, sumo-TDP-43-$^{1-274}$, His-TDP-43$^{1-274}$, His-TDP-43$^{1-274}$-ΔRRM1, His-TDP-43$^{1-274}$-ΔRRM2 and His-TDP-43$^{1-274}$-D169G constructs were generated by PCR using the above WT or mutant TDP-43 plasmid as a template and were sub-cloned into a pET28a-6×His (a gift from Dr. L. Pan) or pET28a-6×His-sumo (a gift from Dr. J. Zhou) vector.

For *in vitro* transcription of NEAT1 RNA, the pcDNA3.1-NEAT1 was generated by PCR using the pEGFP-C1-mNEAT1 plasmid (a gift from Dr. L. Chen) as a template and sub-cloned into the pcDNA3.1 vector.

The primers used for PCR to generate the expression plasmids are summarized below. All constructs were verified by sequencing to ensure the integrity of the cloned open reading frames.

pcDNA3.1-TDP-43-HA:

5'- CGTTTAAACGGGCCCTCTAGAGCCACCATGTCTGAATATATTCGG -3'

5'-CACAGTGGCGGCCGCCTAAGCGTAGTCTGGGACGTCGTATGGGTACATTCCCCAG CCAGAAG -3'

pcDNA3.1-TDP-43-NLS^{mut}-HA:

5'- TAACGCAGCAGCAATGGATGAGACAGATGCTTCATCA -3

5'- CCATTGCTGCTGCGTTATCTTTTGGATAGTTGACAACATACA -3

pcDNA3.1-TDP-43-NES^{mut}-HA:

5'- GGCAGCGCAGTCTGCATGTGGAGAGGACTTGATCATTAAAGG -3

5'- ATGCAGACTGCGCTGCCTGATCATCTGCAAATGTAACAAAGG -3

pLenti-hSyn-TDP-43-HA:

5'- AGAGCGCAGTCGAGAGGATCCGCCACCATGTCTGAATATATTCGG -3'

5'- GATAAGCTTGATATCGAATTCTCATTAAGCGTAGTCTGGGACGTCG -3'

pBID-UASC-TDP-43-Myc:

5'- CGGCCGCGGCTCGAGGGTACCATGTCTGAATATATTCGGGTAACCG -3'

5'- GAGTTTTTGTTCGAAGGGCCCTCTAGACTCGAGCATTCCCCAGCCAGAAGACTT-3'

pBID-UASC-TDP-43-NLS^{mut}-Myc:

5'- CGGCCGCGGCTCGAGGGTACCATGTCTGAATATATTCGGGTAACCG -3'

5'- GAGTTTTTGTTCGAAGGGCCCTCTAGACTCGAGCATTCCCCAGCCAGAAGACTT-3'

pBID-UASC-TDP-43-NES^{mut}-Myc:

5'- CGGCCGCGGCTCGAGGGTACCATGTCTGAATATATTCGGGTAACCG -3'

5'- GAGTTTTTGTTCGAAGGGCCCTCTAGACTCGAGCATTCCCCAGCCAGAAGACTT-3'

pcDNA3.1-TDP-43-K145/192Q-HA:

5'- TCATTCACAGGGGTTTGGCTTTGTTCGTTTT -3

5'- CAAACCCCTGTGAATGACCAGTCTTAAGATCTTTCTTG -3

5’- GCAGACAAGTGTTTGTGGGGCGCTGTAC -3

5’- CACAAACACTTGTCTGCTTCTCAAAGGCTCATCTT -3

pcDNA3.1-TDP-43-NES^{mut}-K145/192R-HA:

5’- TCATTCAAGGGGGTTTGGCTTTGTTCGTTTT -3

5’- CAAACCCCCTTGAATGACCAGTCTTAAGATCTTTCTTG -3

5’- GCAGAAGAGTGTTTGTGGGGCGCTGTAC -3

5’- CACAAACACTCTTCTGCTTCTCAAAGGCTCATCTT -3

pcDNA3.1-TDP-43-D169G-HA:

5’- ATGATAGGTGGACGATGGTGTGACTGCAAACT -3’

5’- CATCGTCCACCTATCATATGTCGCTGTGACATTACTTTC -3’

pcDNA3.1-TDP-43-M337V-HA:

5’- GGTATGGTGGGCATGTTAGCCAGCCAGCAGAA -3’

5’- AACATGCCCACCATACCCCAACTGCTCTGTAGTGC -3’

pCMV-Myc-TDP-43:

5’- ATGGCCATGGAGGCCCGAATTCATGTCTGAATATATT-3’

5’- CCGCGGCCGCGGTACCTCGAGCTACATTCCCCAGCCAGAAGAC -3’

pCMV-Myc-TDP-43$^{1–274}$:

5’- ATGGCCATGGAGGCCCGAATTCATGTCTGAATATATT -3’

5’- CCGCGGCCGCGGTACCTCGAGCTATCCACTTCTTTCTAACTGTCTATTGC -3’

pCMV-Myc-TDP-43-ΔRRM1:

5’- ATGGCCATGGAGGCCCGAATTCATGTCTGAATATATT -3’

5‘- CCGCGGCCGCGGTACCTCGAGCTACATTCCCCAGCCAGAAGAC -3’

pCMV-Myc-TDP-43-ΔRRM2:

5’- ATGGCCATGGAGGCCCGAATTCATGTCTGAATATATT -3’

5‘- CCGCGGCCGCGGTACCTCGAGCTACATTCCCCAGCCAGAAGAC -3’

pCAG-GFP-TDP-43:

5’- CATCATTTTGGCAAAGAATTCCACCATGGTGAGCAAGGGCGAGG -3’

101 5'- CAGACATGCTTCCGCCCTTGTACAGCTCGTCCATGCC -3'

102 5'- CGAGCTGTACAAGGGCGGAAGCATGTCTGAATATATTCGGGTAACCG -3'

103 5'- GCTCCCCGGGGGTACCTCGAGCTATTACATTCCCCAGCCAGAAGACTT -3'

104 pET28a-6×His-TDP-43$^{1–274}$:

105 5'- CAGCAAATGGGTCGCGGATCCATGTCTGAATATATTCGGGTAACCG -3'

106 5'- GTGGTGGTGGTGGTGCTCGAGTTAACTTCTTTCTAACTGTCTATTGCTATTG -3'

107 pET28a-6×His-TDP-43$^{1–274}$-ΔRRM1:

108 5'- CAGCAAATGGGTCGCGGATCCATGTCTGAATATATTCGGGTAACCG -3'

109 5'- GTGGTGGTGGTGGTGCTCGAGTTAACTTCTTTCTAACTGTCTATTGCTATTG -3'

110 pET28a-6×His-TDP-43$^{1–274}$-ΔRRM2:

111 5'- CAGCAAATGGGTCGCGGATCCATGTCTGAATATATTCGGGTAACCG -3'

112 5'- GTGGTGGTGGTGGTGCTCGAGTTAACTTCTTTCTAACTGTCTATTGCTATTG -3'

113 pET28a-6×His-TDP-43$^{1–274}$-D169G:

114 5'- CAGCAAATGGGTCGCGGATCCATGTCTGAATATATTCGGGTAACCG -3'

115 5'- GTGGTGGTGGTGGTGCTCGAGTTAACTTCTTTCTAACTGTCTATTGCTATTG -3'

116 pET28a-6×His-sumo-TDP-43:

117 5'- AGAGAACAGATTGGTGGATCCATGTCTGAATATATTCGGGTAACCG -3'

118 5'-TTGTCGACGGAGCTCGAATTCTTACATTCCCCAGCCAGAAGAC -3'

119 pET28a-6×His-sumo-TDP-43-$^{1–274}$:

120 5'- AGAGAACAGATTGGTGGATCCATGTCTGAATATATTCGGGTAACCG -3'

121 5'- TTGTCGACGGAGCTCGAATTCTTATCCACTTCTTTCTAACTGTCTATTGC -3'

122 pcDNA3.1-NEAT1:

123 5'- CGTTTAAACGGGCCCTCTAGAGAGTTAGTGACAAGGAGGGCTCG -3'

124 5'- ATATCCAGCACAGTGGCGGCCGCTTCAATCTCAAACCTTTATTTTGCTG-3'

125

126 **Cell cultures and transfection**

127 293T and HeLa cells were cultured in Dulbecco's Modified Eagle Medium (Sigma, D0819)

128 supplemented with 10% (v/v) fetal bovine serum (FBS, BioWest) and 1% penicillin/streptomycin
129 at 37˚C in 5% CO_2. Transient transfection was performed using Lipofectamine™ 3000
130 (Invitrogen) in Opti-MEM (Invitrogen). Cells were transfected for at least 24h before the
131 subsequent drug treatments or examinations.
132
133 **Pharmacological experiments:**
134 Arsenite treatment: HeLa or 293T cells were grown on coverslips in a 24-well plate and
135 transfected with the indicated plasmids for 24 h. Cells were then treated with 250 μM of $NaAsO_2$
136 or PBS for 30 min, prior to fixation with 4% paraformaldehyde. For the recovery experiments, the
137 culture medium containing $NaAsO_2$ was removed and the cells were incubated in fresh medium
138 for indicated time prior to fixation.
139 LMB treatment: For the nuclear export inhibition assays, LMB was added into the culture
140 medium after 6h transfection at indicated final concentrations.
141 CHX treatment: For the pulse-chase assays, CHX was added into the medium at each time
142 point at a final concentration of 25 ng/ml.
143 MG132 treatment: For the proteasomal inhibition assays, MG132 was added into the
144 medium at each time at a final concentration of 25 μM.
145 CQ treatment: For autophagy inhibition assays, CQ was added into the medium at each time
146 at a final concentration of 25 mM.
147 The cells incubated in the culture medium with the above drugs for indicated time before
148 fixation for immunocytochemistry or western blotting analysis.
149
150 **Immunocytochemistry and immunohistochemistry assays**
151 HeLa or 293T cells grown on coverslips pre-coated with PLL (Sigma) in a 24-well plate were
152 transfected and treated as described above. The cells were then fixed in 4% paraformaldehyde
153 in PBS for 15 min at room temperature (RT), permeabilized in 0.5% Triton X-100 (Sigma) in PBS
154 for 15 min and blocked with 3% goat serum in PBST (0.1% Triton X-100 in PBS) for 1h at RT.

155 For immunostaining of the whole-mount *Drosophila* brain, fly brains were dissected on ice
156 and immediately fixed in 4% paraformaldehyde in PBS for 30 min at RT and permeabilized with
157 0.5% Triton X-100 in PBS overnight at 4°C overnight.
158 The above primary and secondary antibodies were then incubated in the blocking buffer at
159 4°C overnight or at RT for 1-2 h. After 3 washes with PBST, cells were mounted on glass slides
160 using the VECTASHIELD Antifade Mounting Medium with DAPI (Vector Laboratories).
161

162 **Confocal and super-resolution imaging**

163 Fluorescent confocal images were taken with Leica TCS SP8 confocal microscopy system using
164 a 63X or 100X oil objective (NA=1.4). Super-resolution images were captured using the Leica
165 SP8 LIGHTNING confocal microscope, which allowed simultaneous multicolor imaging in
166 super-resolution down to 120 nm. Confocal or super-resolution images were then processed in
167 LAS X (Leica) and assembled into figures using Adobe Photoshop CS6.
168

169 **Live cell imaging**

170 HeLa cells transfected with pCAG-GFP-TDP-43 were grown on Nunc™ Lab-Tek™ Chambered
171 Coverglass (Thermo) for 24 h before the cells were treated with 250 μM of $NaAsO_2$. For live cell
172 imaging, the chambered coverglasses were placed in the Incubation System for Microscopes
173 (Tokai Hit) and maintained at 37˚C in 5% CO_2 for the duration of the experiment. Time-lapse
174 images were captured using the Leica TCS SP8 confocal microscopy system every 10 min for
175 about 1 h.
176

177 **Fluorescence recovery after photobleaching (FRAP) assay**

178 The PFRP assay was performed using the FRAP module of the Leica SP8 confocal microscopy
179 system. In brief, each GFP-TDP-43 NB was bleached using a 488 nm laser at 100% laser power
180 for approximately 5 s. After photobleaching, time-lapse images were captured every 10 s for the
181 about 5 min. For each indicated time point (t), the fluorescence intensity within the bleached NB

182 was normalized to the fluorescence intensity of a nearby, unbleached NB (to control for
183 photobleaching during prolonged live imaging). The normalized fluorescence intensity of
184 pre-bleaching was set to 100% and the normalized fluorescence intensity at each time point (I_t)
185 was used to calculate the fluorescence recovery according to the following formula: FR(t) =
186 $I_t/I_{pre\text{-}bleaching}$. Image J was used for quantification and GraphPad Prism to plot and analyze the
187 FRAP experiments.
188

189 **Antibodies**

190 The following antibodies were used for Western blotting, immunoprecipitation and
191 immunofluorescence assays: mouse anti-FLAG (Sigma, F3165), mouse anti-HA (Proteintech,
192 66006-1), rabbit anti-c-Myc (Sigma, c3956), rabbit anti-TDP-43 (Proteintech, 10782-2-AP),
193 anti-β-Tubulin III (Sigma, T2200), rabbit anti-TIAR (Cell Signaling Technology, 8509S), rabbit
194 anti-SC35 (Abcam, ab204916), rabbit anti-SFPQ (Abcam, ab177149), rabbit anti-TAF9 (Abcam,
195 ab169784), rabbit anti-PML (Abcam, ab179466), and chicken anti-MAP2 (Abcam, ab5392). HRP
196 conjugated secondary antibodies: goat anti-mouse (Sigma, A4416) and goat anti-rabbit (Sigma,
197 A9169). Fluorescent secondary antibodies: goat anti-mouse-Alexa Fluor 488 (Life Technologies,
198 A11029), goat anti-rabbit-Alexa Fluor 568 (Life Technologies, A11036) and goat
199 anti-Chicken-Alexa Fluor 568 (Life Technologies, A11041).
200

201 **Protein extraction and Western blotting**

202 Total protein was extracted from cells in a 2% SDS extraction buffer (50 mM Tris pH 6.8, 2%
203 SDS, 1% mercaptoethanol, 12.5% glycerol and 0.04% bromophenol blue) containing the
204 protease inhibitor cocktail (Roche, 04693132001). For separation of soluble and insoluble
205 proteins, cells or fly heads were lysed on ice in a RIPA buffer (50 mM Tris pH 8.0, 150 mM NaCl,
206 1% NP-40, 5 mM EDTA, 0.5% sodium deoxycholate, 0.1% SDS) supplemented with protease
207 and phosphatase inhibitors (Roche). After sonication, the homogenates were centrifuged at
208 16,000 g for 15min at 4°C. The supernatant was used as the soluble fraction and the pellets

209 containing the insoluble fraction were dissolved in a urea buffer (9 M urea, 50 mM Tris buffer, pH
210 8.0) after wash.
211 All protein samples were then boiled at 100°C for 5 min and separated using a 10% Bis-Tris
212 SDS-PAGE (Invitrogen). Detection was performed using the High-sig ECL Western Blotting
213 Substrate (Tanon). Images were captured using an Amersham Imager 600 (GE Healthcare) and
214 densitometry was measured using ImageQuant TL Software (GE Healthcare). The contrast and
215 brightness were optimized equally using Adobe Photoshop CS6. All experiments were
216 normalized to tubulin or GAPDH as indicated in the figures.
217
218 **Cell viability assay**
219 Transfected 293T cells were seeded in 96-well plates (Corning) at the density of 9×10^3 cells/well
220 and cultured in 100 μL of culture medium. Otherwise, cell viability was examined 48-72 h after
221 transfection using the Cell Counting Kit-8 (CCK-8) (Dojindo), according to the manufacturer's
222 instructions. Briefly, 10 μL of the CCK-8 solution were added to each well and incubated at 37°C
223 for 2.5 h. Finally, the absorbance at 450 nm was measured with a Synergy2 microplate reader
224 (BioTek Instruments).
225
226 **Mouse care and surgical procedures**
227 All mouse procedures were performed in compliance with the institutional guidelines on the
228 scientific use of living animals at Interdisciplinary Research Center on Biology and Chemistry,
229 the Chinese Academy of Sciences (CAS). "Principles of laboratory animal care" (NIH publication
230 No. 86-23, revised 1985) were followed. Animal distress and conditions requiring euthanasia
231 were addressed and the number of animals used was minimized.
232
233 **Lentivirus production and primary neuron culture**
234 To generate lentivirus for infecting primary neurons, 293T cells were co-transfected with
235 pLenti-hSyn-TDP-43-HA, psPAX2 and pMD2.G with a ratio of 4:2:1 in Opti-MEM medium using

236 Lipofectamine™ 2000. Culture supernatant was collected at 48 h after transfection and passed
237 through a 0.45-μm filter. Viral particles were concentrated from culture supernatants by Lenti-X™
238 Concentrator (Clontech). Viral pellets used for neuronal infection were resuspended in
239 Neurobasal medium (Invitrogen).

240 Primary cortical neuron were isolated from C57BL/6 mouse cortex at embryonic day 17 (E17)
241 and cultured in serum-free Neurobasal medium (Invitrogen) supplemented with 2% B27,
242 GlutaMax, and penicillin-streptomycin (Invitrogen). At 7 days in vitro (DIV), neurons were
243 infected with pLenti-hSyn-TDP-43-HA for 5 days before extraction for RNA or
244 immunofluorescence.

245

246 **RNA extraction and real-time quantitative PCR**

247 For quantitative PCR (qPCR), total RNA was isolated from mouse primary neuron using TRIzol
248 (Invitrogen) according to the manufacturer's instruction. After DNase (Promega) treatment, the
249 reverse transcription reactions were performed using All-in-One cDNA Synthesis SuperMix kit
250 (Bimake). The cDNA was then used for real-time qPCR using the SYBR Green qPCR Master Mix
251 (Bimake) with the QuantStudio™ 6 Flex Real-Time PCR system (Life Technologies). The mRNA
252 levels of GAPDH were used as an internal control to normalize the mRNA levels of NEAT1. The
253 qPCR primers used in this study are listed below:

254 Total mNEAT1:

255 5'- ACTCTTGCCCCTCACTCTGA -3'

256 5'- CAGGGTGTCCTCCACCTTTA -3';

257 mNEAT1_2:

258 5'- CCCACACCTCAGTGGTTTCT -3'

259 5'- ACAGAACCAAGGCACAATCC -3';

260 mGAPDH:

261 5'- CACCATCTTCCAGGAGCGAG -3'

262 5'- CCTTCTCCATGGTGGTGAAGAC -3';

263

264 **Purification of TDP-43 proteins**

265 WT or mutant TDP-43 protein was expressed in BL21 (DE3) *E. coli* (TransGenBiotech,
266 CD601-03) at 19°C for 16 h after induction by adding 100 μM of IPTG as previously described
267 (*46*). In brief, cells were harvested by centrifugation at 4000 rpm for 20 min at 4 °C and lysed in
268 50 mL of lysis buffer (50 mM Tris-HCl, 500 mM NaCl, pH 8.0, 10 mM imidazole, 4 mM
269 β-mercaptoethanol, 1 mM PMSF, and 0.1 mg/mL RNase A). After cell lysates were filtered with a
270 0.22 μm filter, the protein was purified using Ni columns (GE Healthcare, USA) and then eluted in
271 an elution buffer (50 mM Tris-HCl, 500 mM NaCl, pH 8.0, 250 mM imidazole and 4 mM
272 β-mercaptoethanol). The proteins were further purified using the Superdex 200 16/600 columns
273 (GE Healthcare) in a buffer containing 50 mM Tris-HCl pH 7.5, 300 mM NaCl and 2 mM DTT,
274 and freshly frozen in liquid nitrogen and stored at -80 °C. RNase A was routinely added in cell
275 lysates and administrated again before chromatography during the protein purification procedure.
276 All purified proteins were confirmed by Coomassie brilliant blue staining and Western blotting
277 before use.

278

279 **RNA-binding dot-blot assay**

280 Purified WT or mutant TDP-43 protein was diluted in a blotting buffer (50 mM Tris-HCl, pH 7.5,
281 300 mM NaCl, and 5% glycerol) and blotted onto a 0.45 μm nitrocellulose membrane. The
282 membranes were left to dry at room temperature for 30 min and then stained with Ponceau S for
283 10s. Images were captured using an Amersham Imager 600 (GE Healthcare). After the images
284 were captured using an Amersham Imager 600 (GE Healthcare), the membranes were washed
285 with PBST (0.05% TWEEN 20 in PBS) for 30 min and then incubated in the PBST containing 25
286 ng/μl total RNAs or NEAT1 RNA for 1h with gentle rocking and rotation at room temperature. The
287 membranes were then washed in PBST and incubated in the SYBR™ Gold Nucleic Acid Gel
288 Stain (Invitrogen) for 10 min. RNAs bound to the membranes were imaged and examined using
289 the Gel Image System (Tanon).

290

291 ***In vitro* phase separation and RNA buffering assay**

292 For the *in vitro* LLPS experiments, purified WT or mutant TDP-43 protein was mixed with NaCl at
293 indicated concentrations in a phase separation buffer (50 mM Tris-HCl, pH 7.5 and 5-10% (w/v)
294 PEG 8000 (Sigma)) and incubated for 1 min at room temperature. For the RNA buffering assay,
295 the TDP-43 proteins were incubated with total RNAs, tRNA or NEAT1 RNA in the above phase
296 separation buffer with NaCl at indicated concentrations as shown in the figures. Finally, 5 μL of
297 each sample was pipetted onto a coverslip and imaged using a Leica microscope with differential
298 interference contrast (DIC). The total RNAs were extracted from HeLa cells using TRIzol
299 (Invitrogen) according to the manufacturer's instructions. Yeast tRNA was purchased from
300 Invitrogen. The NEAT1 RNA was *in vitro* transcribed and purified using HiScribe™ T7 Quick High
301 Yield RNA Synthesis Kit (NEB). Total RNAs and NEAT1 RNA were used within one day of
302 production.

303

304 ***Drosophila* strains**

305 Flies tested in this study were raised on standard cornmeal media and maintained at 25 °C and
306 60% relative humidity. The following strains were obtained from the Bloomington *Drosophila*
307 Stock Center (BDSC): *D42*-Gal4 (#8816), *elav*-Gal4 (#8760) and UAS-*LacZ* (#8529). The
308 transgenic fly strains of WT and mutant UAS-hTDP-43 were generated by ΦC31
309 integrase-mediated, site-specific integration, which allowed uniform transgene expression across
310 different lines. The attP2 landing site stock used for the fly embryo injection and transformation in
311 this study was y[1] M{vas-int.Dm}ZH-2A w[*]; P{CaryP}attP40 (25C6), and the transgenic
312 pBID-UASC-Luciferase (UAS-Luc) fly strain that was generated using the same approach at the
313 same landing site (*100*) was used as a control.

314

315 **Fly climbing assay**

316 For the climbing assay, ~20 flies per vial, ~10 vials per group were tested. All flies were

transferred into an empty polystyrene vial and allowed 10 min for flies to recover. The flies were then gently tapped down to the bottom of the vial and the number of flies that climbed over 3cm within 10 seconds was recorded. The test was repeated three times for each via.

Statistical Analysis

Statistical significance in this study is determined by one-way analysis of variance (ANOVA) with Tukey's HSD post-hoc test, two-way ANOVA with Bonferroni's post-hoc test, or unpaired, two-tailed Student's *t*-test with unequal variance at $*p < 0.05$, $**p < 0.01$, and $***p < 0.001$ as indicated in each figure legend. Error bars represent the standard error of the mean (SEM).

326 **Supplementary Figures**

327

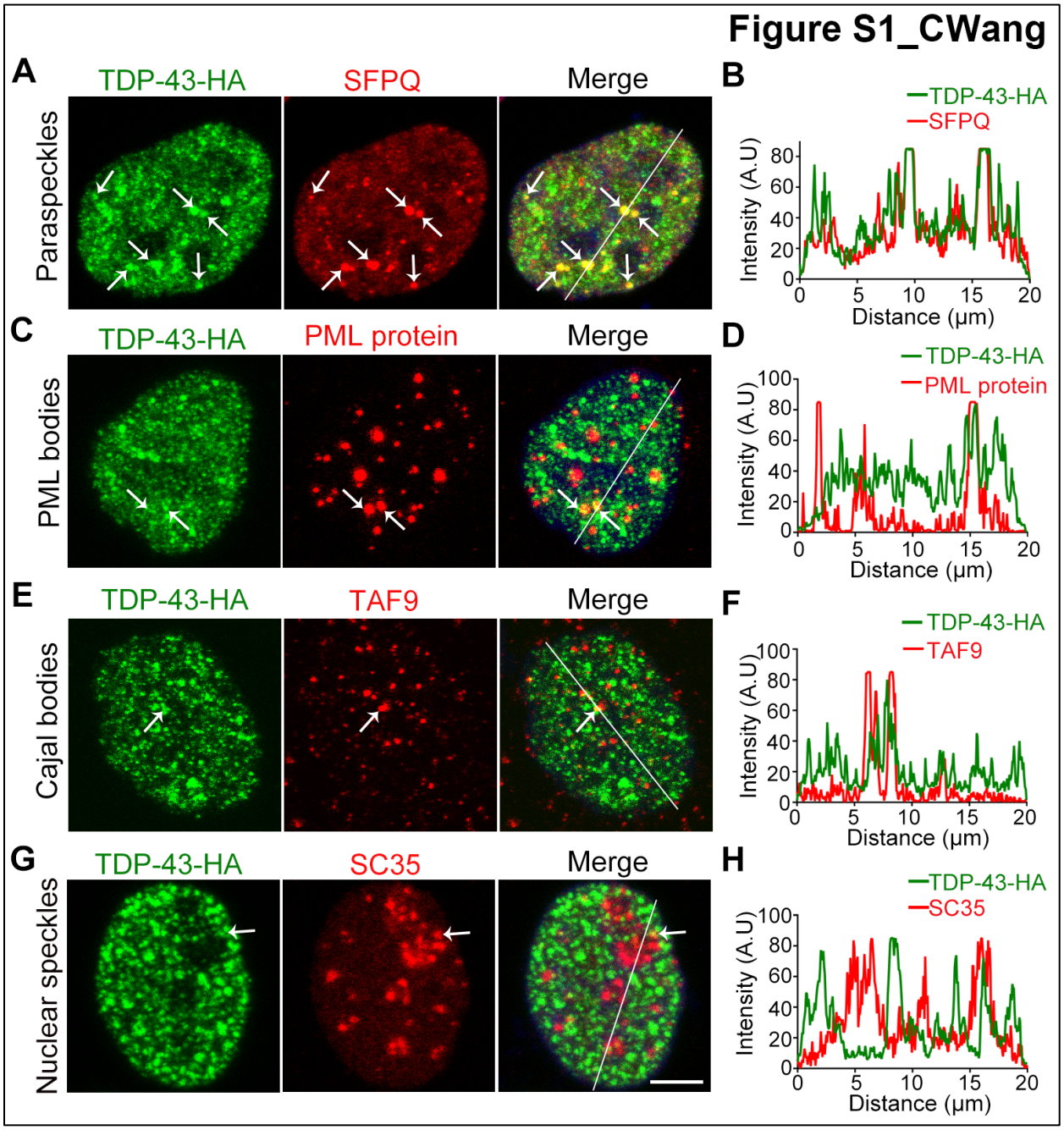

328

329 **Figure S1. Co-immunostaining of TDP-43 with several known NB markers**
330 Representative confocal images of the nucleus of 293T cells transfected with TDP-43-HA and
331 treated with 250 μM $NaAsO_2$ for 30 min. All cells are examined by immunocytochemistry with
332 anti-HA for TDP-43-HA (green) and the indicated antibodies (red): (**A-B**) SFPQ (splicing factor
333 proline-glutamine rich), for paraspeckles (*74*). (**C-D**) PML (promyelocytic leukaemia) protein, for
334 PML bodies (*101*). (**E-F**) TAF9 (TATA-box binding protein associated factor 9) for Cajal bodies
335 (*102*). (**G-H**) SC35 (serine/arginine-rich splicing factor-like protein), for nuclear speckles (*103*).
336 Merged images with DAPI staining (for DNA) are shown. Arrows indicate the examples of
337 co-localization of TDP-43 with the indicated NB markers. The co-localization of TDP-43 with
338 each type of NBs is further evaluated by the line scanning analysis shown in (B), (D), (F) and (H),
339 Scale bar: 5 μm. The results indicate that TDP-43 NBs are well colocalized with paraspeckles,
340 and in a few rare cases partial colocalization with PML bodies, Cajal bodies or nuclear speckles
341 are also spotted.

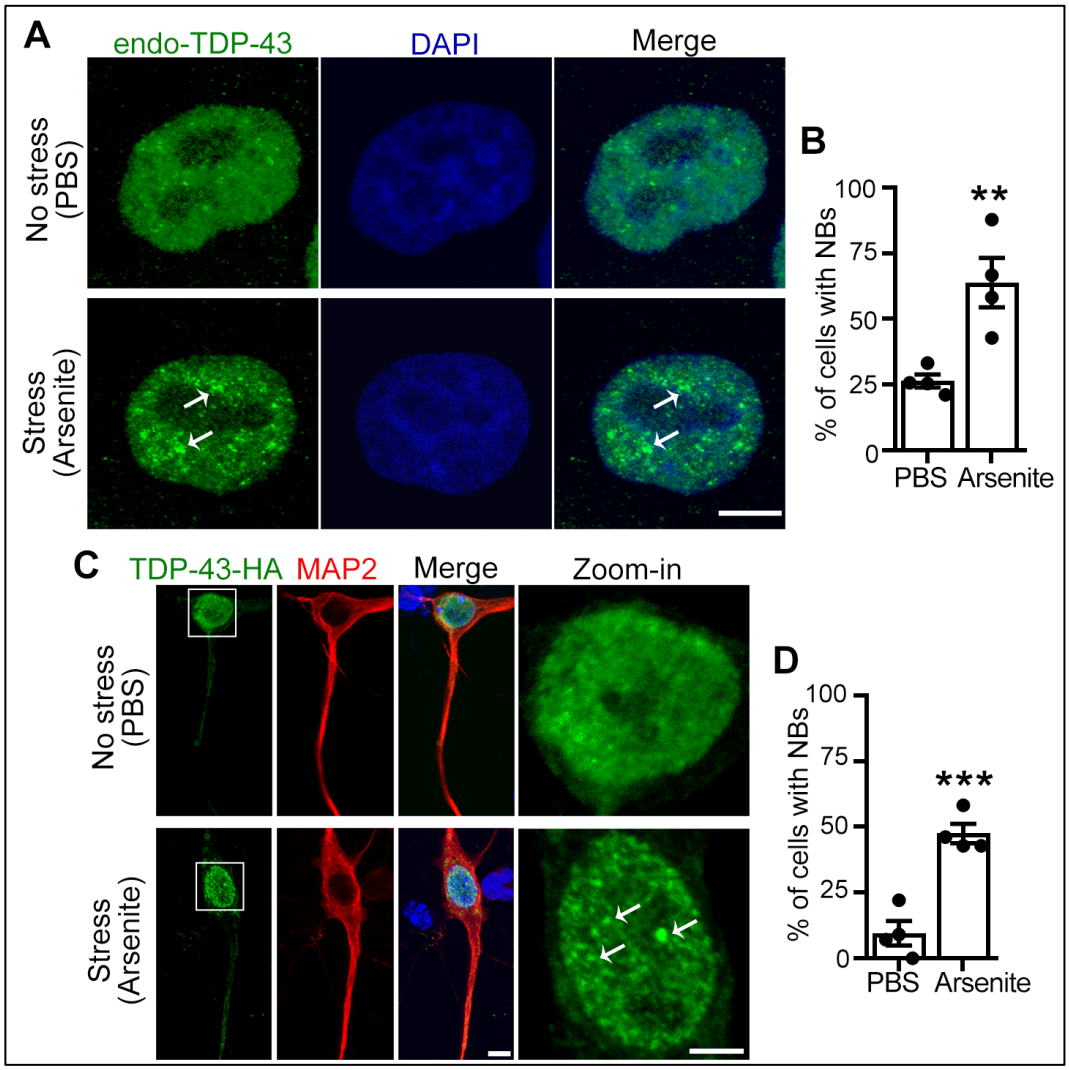

Figure S2. Stress-induced NBs are observed with endogenous TDP-43 and in primary neurons

(**A-B**) Representative images of endogenous TDP-43 (endo-TDP-43) forming NBs upon arsenite treatment (500 μM, 30 min). DAPI staining to show the nucleus and merged images are also shown. Percentage of cells showing distinct TDP-43 NBs in (A) is quantified in (B). Arrows indicate TDP-43 NBs. (**C-D**) Representative images (C) and quantification (D) of TDP-43-HA NBs in primary mouse cortical neurons induced by arsenite treatment. TDP-43-HA (green), microtubule associated protein 2 (MAP2) to mark neuronal perikarya and dendrites (red), and merged images with DAPI staining to label the nucleus (blue) are shown. Zoom-in images of the boxed areas are also shown. Mean ± SEM, n = 100 cells each group from pooled results of 3 independent repeats; $^{**}p < 0.01$, $^{***}p < 0.001$; Student's *t*-test. Scale bars: 5 μm in (A and C), and 2 μm in the zoom-ins.

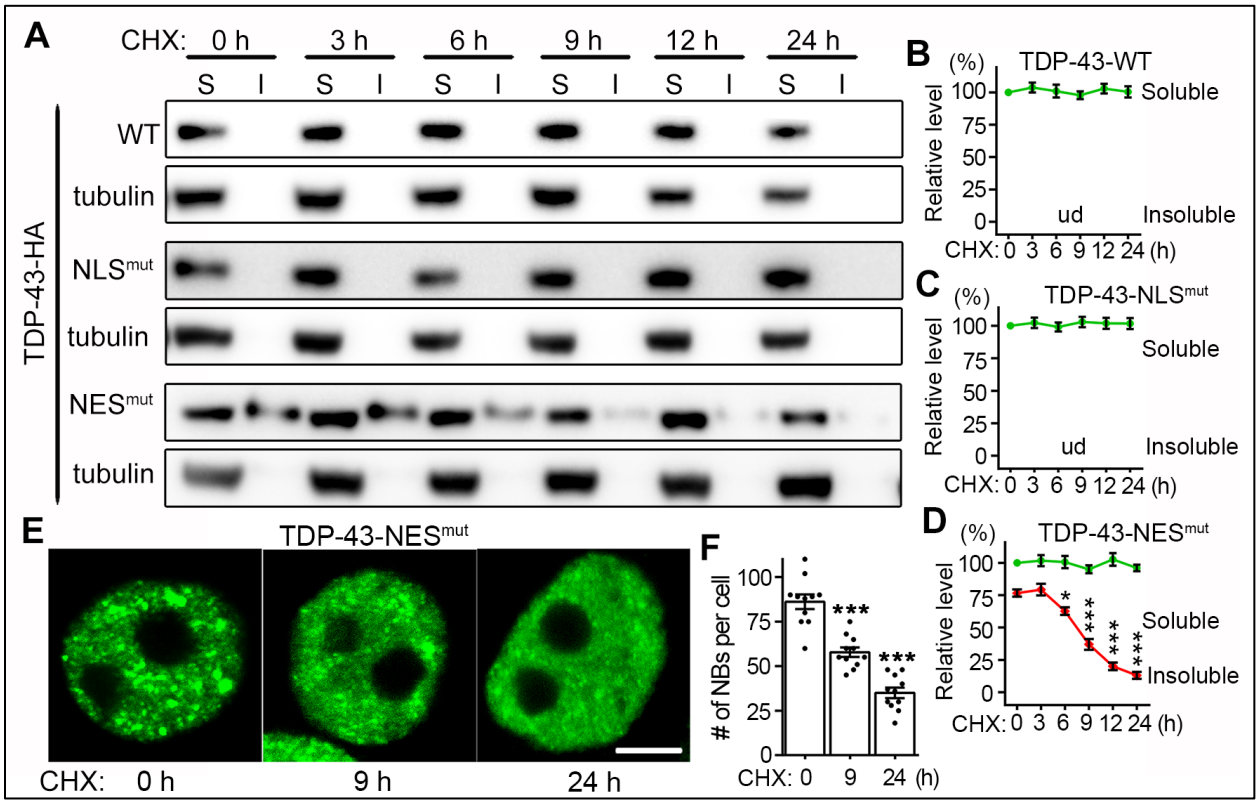

Figure S3. TDP-43-NES^{mut} NBs are dynamic and reversible

(**A-D**) Representative Western blot images (A) and quantifications (B-D) of the pulse-chase experiments of WT, NLS^{mut} and NES^{mut} TDP-43 protein in the soluble (S, supernatants in RIPA) and the insoluble (I, pellets resuspended in 9 M of urea) fractions at indicated time after Cycloheximide (CHX) treatment. All proteins are normalized to tubulin in the soluble fraction and the relative level at 0 h is set to 100%. Mean ± SEM, n = 3 independent repeats; compared to the level at 0 h; *P < 0.05, ***P < 0.001; ud, undetected; one-way ANOVA. (**E**) Representative images showing TDP-43-NES^{mut} NBs in 293T cells at indicated time after CHX treatment. (**F**) Quantification of the average number of TDP-43 NBs per cell in (E). Mean ± SEM, n = 10~11 cells per time point, from pooled results of 3 independent repeats; ***p < 0.001; one-way ANOVA. Scale bar: 5 μm.

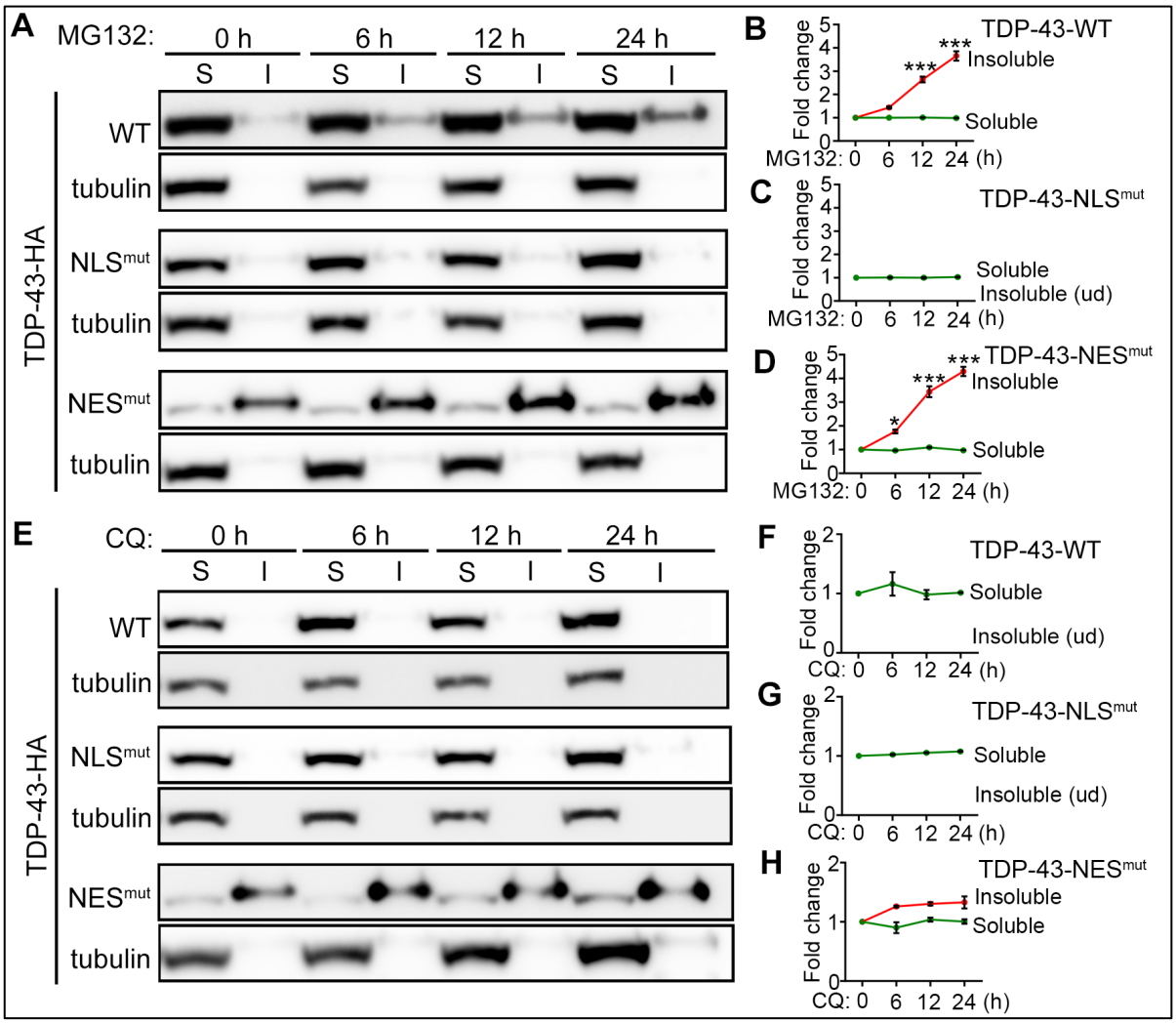

Figure S4. The turnover of insoluble TDP-43 is sensitive to proteasomal but not autophagic inhibition

(**A-D**) Representative images (A) and quantifications (B-D) of Western blotting analyses of WT, NLS^{mut} and NES^{mut} TDP-43 in the soluble (S) and insoluble (I) fractions at indicated time after treating the cells with MG132 to inhibit the proteasome-mediated protein degradation. (**E-H**) Representative images (E) and quantifications (F-H) Western blot analyses of WT, NLS^{mut} and NES^{mut} TDP-43 in the soluble (S) and insoluble (I) fractions at indicated time after treating the cells with chloroquine (CQ) to block the autophagic flux. S, supernatants in RIPA; I, precipitates in RIPA that are re-suspended in 9 M of urea. All proteins are normalized to tubulin in the soluble fraction and the relative level of each fraction at 0 h is set to 1. Mean ± SEM, n = 3 independent repeats; *$P < 0.05$, ***$p < 0.001$; ud, undetected; one-way ANOVA.

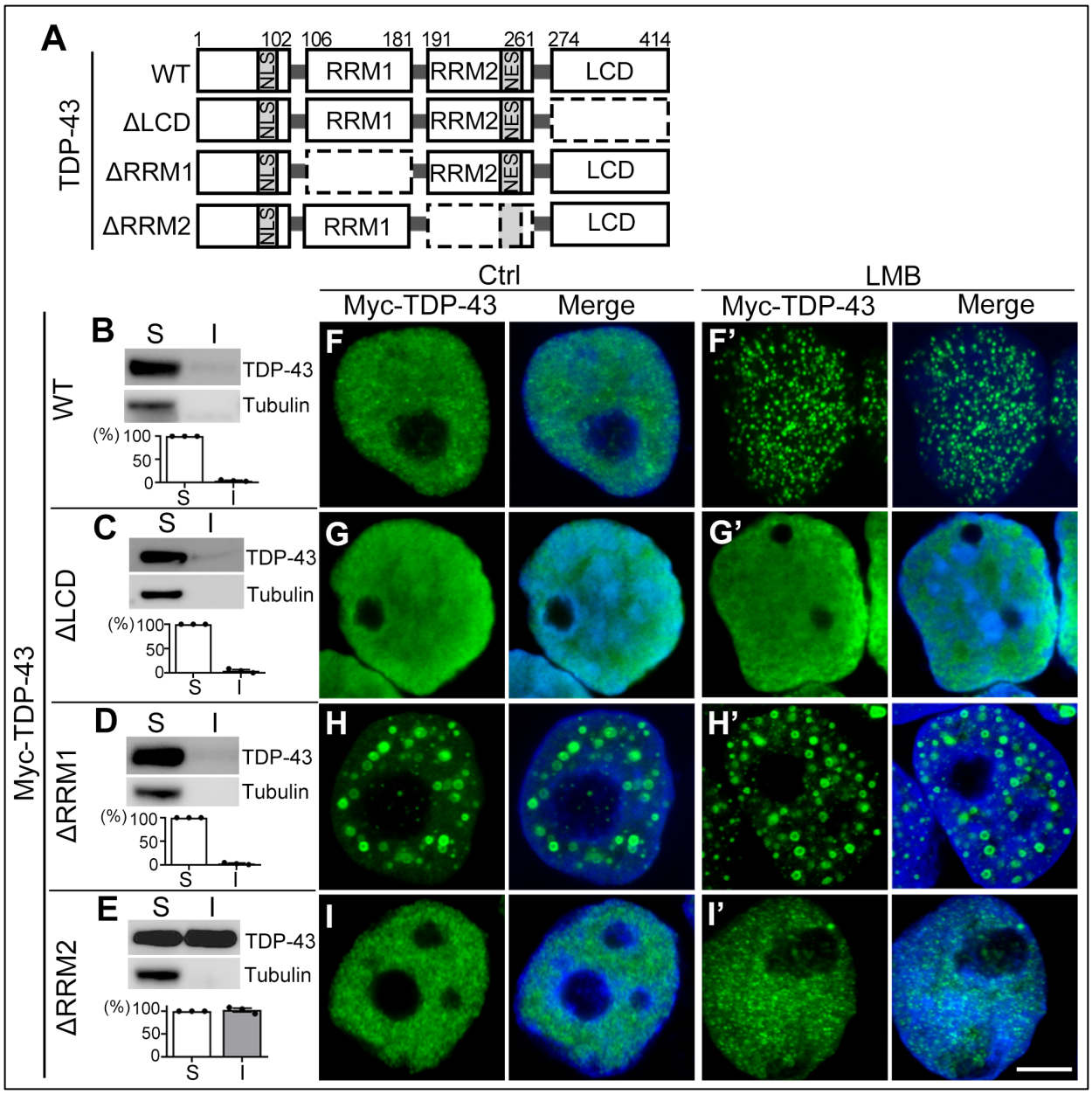

379

380 **Figure S5. The impact of the LCD and RRM domains on the assembly of TDP-43 NBs**
381 (**A**) A diagram showing the major functional domains and the truncated ΔLCD, ΔRRM1 and
382 ΔRRM2 TDP-43. (**B-E**) Western blot analysis of TDP-43-WT (B), ΔLCD (C), ΔRRM1 (D) and
383 ΔRRM2 (E) in the RIPA-soluble and RIPA-insoluble (resuspended in 9 M of urea) fractions. All
384 TDP-43 proteins are normalized to tubulin in the soluble fraction and the relative level is
385 quantified as percentage to the soluble fraction of each protein. Mean ± SEM, n = 3 independent
386 repeats. (**F-I'**) Representative confocal images of TDP-43-WT, ΔLCD, ΔRRM1 and ΔRRM2 in
387 293T cells treated with the vehicle control ethanol (F-I) or LMB (F'-I'). Green, anti-Myc for
388 Myc-TDP-43; blue, DAPI for DNA. Scale bar: 5 μm.

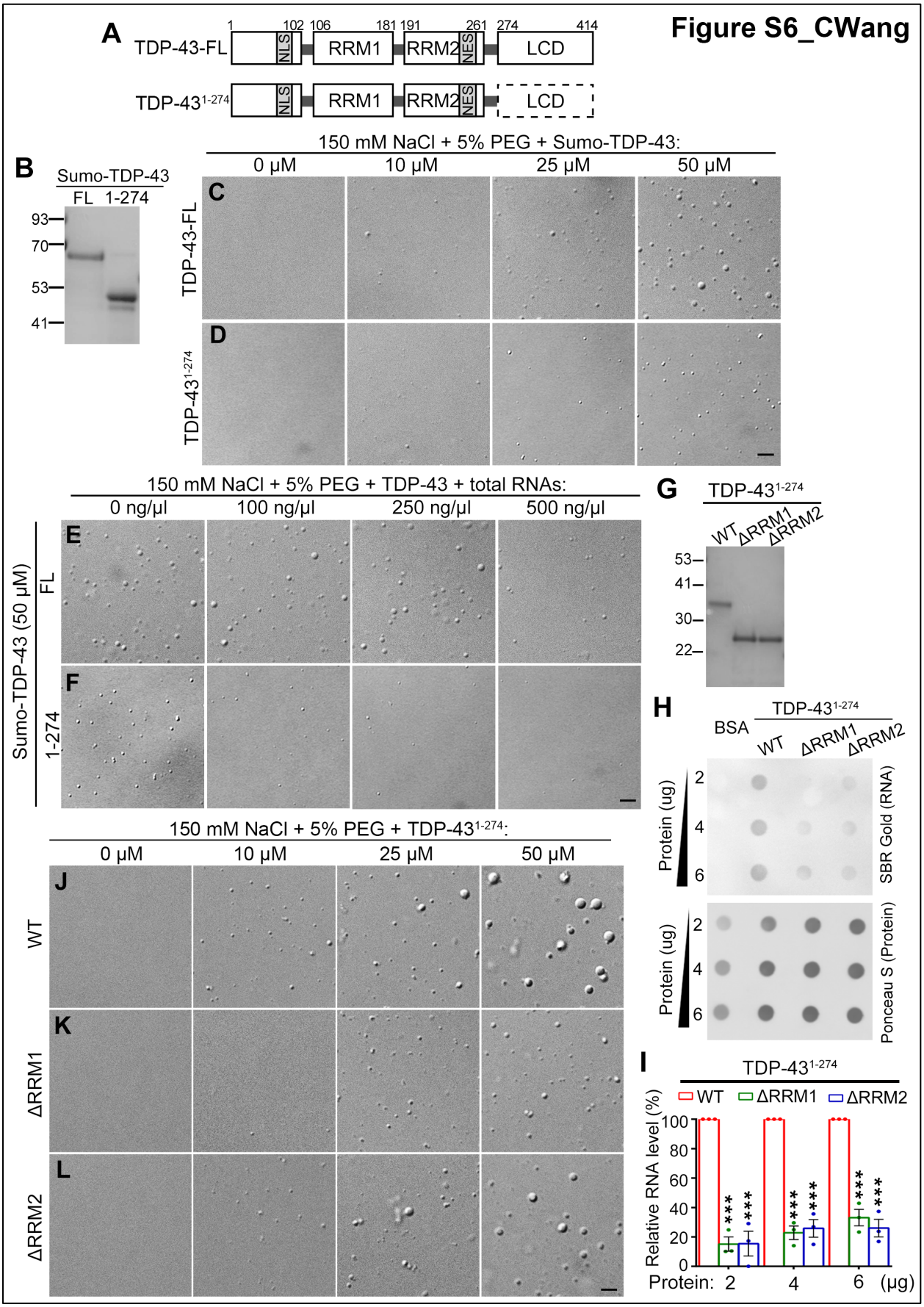
Figure S6_CWang
A
TDP-43-FL
1
102
106
181
191
261
274
414
NLS
RRM1
RRM2
NES
LCD
TDP-43 1-274
B
Sumo-TDP-43
FL
1-274
93
70
53
41
150 mM NaCl + 5% PEG + Sumo-TDP-43:
0 μM
10 μM
25 μM
50 μM
C
D
TDP-43-FL
TDP-43 1-274
150 mM NaCl + 5% PEG + TDP-43 + total RNAs:
0 ng/μl
100 ng/μl
250 ng/μl
500 ng/μl
E
F
Sumo-TDP-43 (50 μM)
FL
1-274
G
TDP-43 1-274
WT
ΔRRM1
ΔRRM2
53
41
30
22
H
BSA
TDP-43 1-274
WT
ΔRRM1
ΔRRM2
Protein (ug)
2
4
6
SBR Gold (RNA)
Ponceau S (Protein)
150 mM NaCl + 5% PEG + TDP-43 1-274:
0 μM
10 μM
25 μM
50 μM
J
K
L
WT
ΔRRM1
ΔRRM2
I
TDP-43 1-274
WT
ΔRRM1
ΔRRM2
Relative RNA level (%)
100
80
60
40
20
0
***
Protein: 2
4
6
(μg)

389

390 **Figure S6. Total RNAs suppress TDP-43 LLPS *in vitro***

391 (**A**) A diagram showing the full-length (FL) and truncated TDP-43 protein without the LCD
392 (TDP-43^{1-274}). (**B**) Coomassie blue staining confirming the purified FL and truncated
393 sumo-TDP-43 proteins. (**C-D**) The *in vitro* LLPS of FL (C) and TDP-43^{1-274} (D) is dose-dependent.
394 (**E-F**) Suppression of the LLPS of the FL and the TDP-43^{1-274} by total RNAs extracted from HeLa.
395 (**G**) Coomassie blue staining confirming purified WT, ΔRRM1 and ΔRRM2 TDP-43^{1-274} proteins
396 used in the *in vitro* assays below and in Figure 6. (**H**) Representative images of the *in vitro*
397 dot-blot assay confirming the reduced RNA binding affinity of the ΔRRM1 and ΔRRM2
398 TDP-43^{1-273} compared to the WT. The bound RNA is visualized using the SYBR® Gold Nucleic
399 Acid Gel Stain kit. Bovine serum albumin (BSA) is used as a negative binding control. (**I**) The
400 RNA intensity is normalized to Ponceau S staining (protein loading control) and shown as the
401 percentage to that of WT TDP-43^{1-273} in (H). Mean ± SEM, n = 3; ***$p < 0.001$; Student's *t*-test.
402 (**J-L**) WT (J), ΔRRM1 (K) and ΔRRM2 (L) TDP-43^{1-273} proteins forms LDs *in vitro* by LLPS in a
403 dose-dependent manner. The concentrations of NaCl, the crowding agent PEG, TDP-43 protein
404 and total RNAs used in the above assays are as indicated. Scale bars: 2 μm.

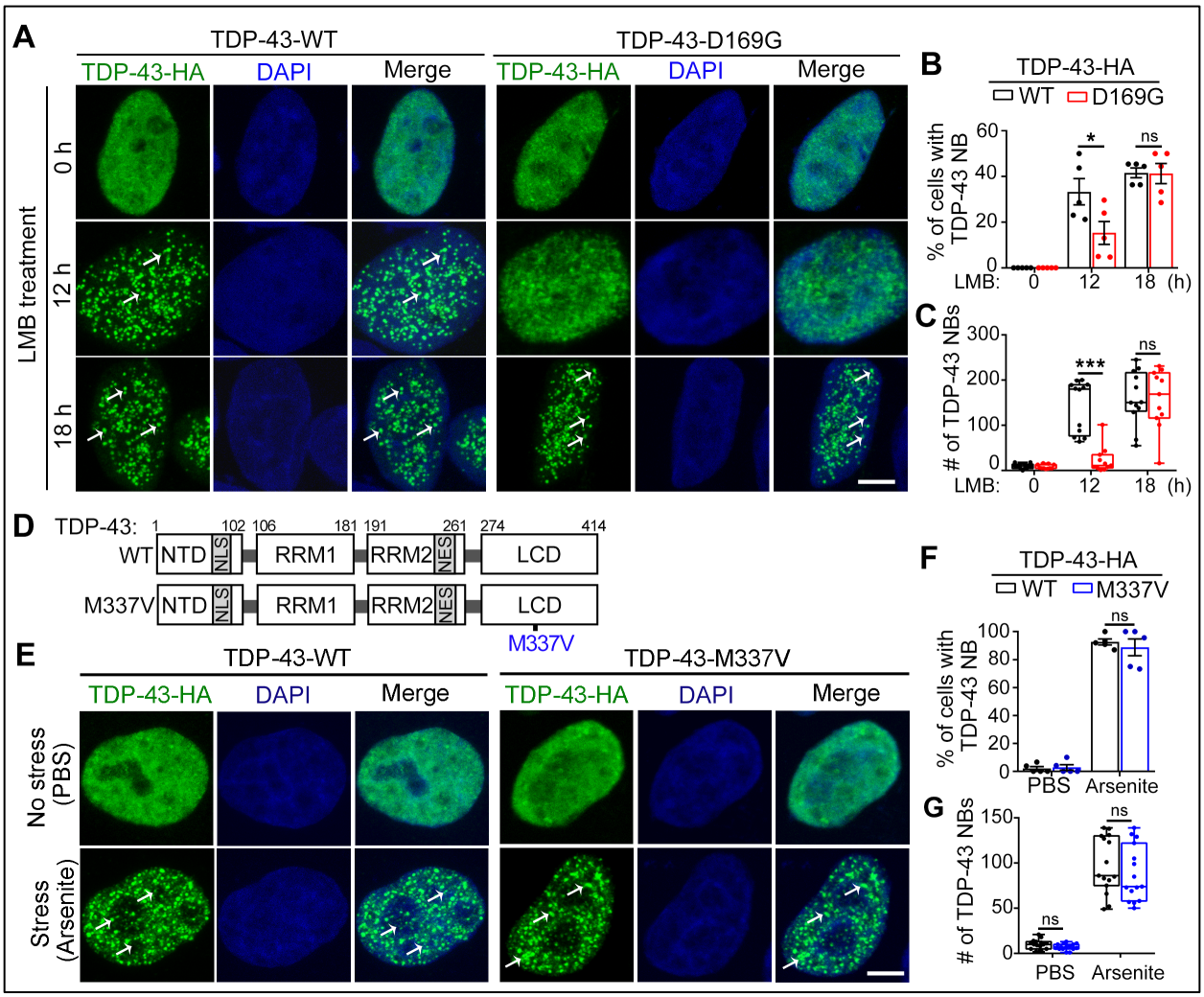

Figure S7. The D169G mutant TDP-43 has a specific defect in NB formation

(**A**) Representative confocal images of HeLa cells expressing with WT or D169G TDP-43 treated with LMB for indicated times. (**B-C**) Quantifications of the percentage of cells showing TDP-43 NBs (B) and the average number of NBs per cell (C) at the end of the experiment in (A). LMB-induced NB formation was delayed in D169G TDP-43. (**D**) A diagram showing WT TDP-43 and the M337V mutation in the LCD. (**E**) Representative confocal images of cells transfected with WT or M337V TDP-43 in the absence (PBS) or presence of arsenite. Green, TDP-43-HA (anti-HA); Blue, DAPI staining for DNA (blue); arrows, TDP-43 NBs. (**F-G**) The percentage of cells with TDP-43 NBs (F) and the average count of TDP-43 NBs per cell (G) in (E) are quantified. Mean ± SEM, n = ~100 cells in total for each group in (B, F) and 11~15 cells per group in (C, G), pooled results from 3 independent repeats; *$p < 0.05$, ***$p < 0.001$; ns, not significant; Student's *t*-test. Scale bars: 5 μm.

418 ## Supplementary movies

419

420 **Movie S1. A representative time-lapse video of *live* HeLa cells showing the formation of**
421 **GFP-TDP-43 NBs upon the arsenite treatment**

422

423 **Movie S2. A representative time-lapse video of GFP-TDP-43-GFP NBs in *live* HeLa cells**
424 **before and after photobleaching**